CENTRO DE INVESTIGACIONES EN ÓPTICA, A.C.

Handling supercontinuum in the femtosecond regime by spectra generation and by optimization with genetic algorithms

Doctorado en Ciencias (Óptica)

Asesor(es):

Dr. Ismael Torres Gómez

Dr. Miguel Torres Cisneros

Estudiante:

MI. Francisco Rodrigo Arteaga Sierra

Noviembre de 2014

León, Guanajuato, México

Handling supercontinuum in the femtosecond regime by spectra generation and by optimization with genetic algorithms

M.Eng. Francisco R. Arteaga-Sierra

Photonics Division

Center for Research in Optics

Thesis submitted in partial fulfillment of the requirements for the degree of

Doctor of Science (Optics)

León, Guanajuato, México, November 2014.

Supervisors

Ph.D. Ismael Torres-Gómez, Center for Research in Optics

Ph.D. Miguel Torres-Cisneros, University of Guanajuato

Day of the defense: Nov 7, 2014.

Abstract

Supercontinuum generation has been the subject of extensive studies in optical fibers and its special spectral shapes are of many interest for a variety of applications. For input pulses in the femtosecond regime, the dynamics of supercontinuum generation generation can be broadly decomposed into two phases: an initial fission into an N soliton dominated by the Kerr effect and second order dispersion; and a subsequent redistribution of spectral energy where the Raman effect and higher dispersion orders also play a role. In this work, these two phases are exploited to numerically handle the spectral output in order to adequately apply the supercontinuum generation phenomenon to medical image techniques, specifically, optical coherence tomography. The First part is focused on the development of methods that use the properties of dispersive waves and the soliton self-frequency shift to obtain simultaneous spectral peaks tuned on specific frequencies, both of them sited on after the initial-fission scenario. Additionally, it is shown a method to obtain an ultra-flat spectrum based on self-phase modulation. The last effect is sited on before the initial-fission scenario. Based on these methods, the results of this thesis show that supercontinuum spectral output can be tailored to bell-shaped pulses to optical coherence tomography applications, ultra-flat to telecommunications or any proposed spectral forms (conditions permitting), resulting in a useful tool with great potential for many practical areas.

Acknowledgements

TO THE INSTITUTIONS THAT SUPPORTED MY STUDIES

Thanks to the CONACYT for the support granted to the scholarship holder, Francisco Rodrigo Arteaga Sierra, under the number of registry 207588, during the period September-2009 to August-2013.

Thanks to the CONCyTEG and DAIP-UG for the scholarship-mix granted to Francisco Rodrigo Arteaga Sierra during the period September-2013 to August-2014, through the partial funding provided by the projects CONCyTEG (GTO-2012-C03-195247) and DAIP-UG 382/2014.

Thanks to the project: Fabricación y aplicación de fibras de cristal fotónico para fuentes de luz supercontinua (106764: CONACYT, CB2008) by the provided partial support.

Contents

List of Figures

List of Tables

1

Introduction

A supercontinuum (SC) is a broad spectrum extending beyond all visible colors with the properties of a laser, i.e. spatial and temporal coherent in all its compound wavelengths. This particular process occurs when narrow-band incident pulses undergo extreme nonlinear spectral broadening to yield a broadband (very often a white light) spectrally continuous output. The first observation of a SC dates to 1970, when Alfano and Shapiro focused powerfully picosecond pulses into a glass sample [1]. Thenceforth, it has been the subject of numerous investigations in a wide variety of nonlinear media, including solids, organic and inorganic liquids, gases, and various types of waveguides. Later, SC generation was achieved in a conventional single mode optical fiber in 1987 [2, 3]. The physics behind the process of SC generation in PCF has been studied since the results of Ranka *et.al.*, and several attempts have been made to explain the generated broad bandwidth [4, 5, 6]. The dominant nonlinear effects responsible for the SC generation are expected to be self-phase modulation(SPM), self-steepening (SS), intrapulse Raman scattering (IRS) and four-wave mixing (FWM). To acquire a better understanding of the physical mechanism of the process, and to study the effects of the SC generation in PCFs, simulations of SC generation in PCFs become more and more significant in this area. Numerical modelling of SC generation in PCF using femtosecond pulses was initially reported by Husakou and Herrmann [7], and the crucial role of soliton fission in the spectral broadening process was highlighted for the first time. That result was followed by a

number of more careful comparisons between experiment and simulation, in both the picosecond [4] and the femtosecond [5] regimes.

In the first SC generation experiments in optical fiber was injected high-power pulses in the visible spectral region into standard silica-based optical fiber with zero group velocity dispersion (GVD) wavelength [8]. Subsequent works, clarified the importance of the mutual interaction between Raman scattering and self-phase modulation (SPM), as well as the role of cross-phase modulation (XPM) and various four-wave-mixing (FWM) processes in providing additional broadening, and in merging discrete generated frequency components to produce a spectrally smooth output [3, 9, 10]. The Raman and SPM-dominated broadening in the above experiments was observed for the case of normal GVD pumping. When pumping in the anomalous GVD regime, however, spectral broadening arises from soliton-related dynamics. Several fiber designs have been proposed to enhance the generated bandwidth. SC generation in photonic crystal fibers (PCF) was demostrated in 1999 by Ranka *et.al.* [11]. It was showed that suitable design of the photonic crystal cladding could shift the zero dispersion wavelength (ZDW) of a PCF to wavelengths shorter than the intrinsic zero ZDW of silica around 1.3μm [12]. Furthermore, reducing the effective area of the propagating mode in this type of fiber enhanced the Kerr nonlinearity relative to a standard fiber, leading to significant new opportunities in nonlinear fiber optics [13]. The design freedom of PCFs has allowed SC generation to be observed over a much wider range of source parameters than it was possible with bulk media or conventional fibers. Because of the evident significance of PCF-generated SC, a complete understanding of the various underlying physical mechanisms is of prime importance.

As seen, SC generation is a complex mechanism where many effects that depend on the associated variables to the laser source and the propagating medium are implied, a simple change in the involved variables can lead to a significant change in the spectral output, therefore its final spectral shape is not expected to be trivial. Therefore, the develop of SC modelling techniques has been of interest for many spectral applications. Among those techniques are the management of effects such as dispersive waves [14], soliton self frequency shift (SSFS) [15], the self-phase modulation (SPM) [16], etc. Based on those techniques, SC light

source finds numerous novel applications in the fields of telecommunications [17], optical metrology [18], and medical science. To mention a few examples, the interest in applying SC sources in dense wavelength-division multiplexing (WDM) transmission by slicing the broad spectrum of SC into hundreds of channels, and utilizing an optical time domain multiplexing technique for each channel, transmission bandwidths of terahertz can be achieved [19]. Also, the use of a SC source in single-shot characterization of fiber optics components has been demonstrated [20]. The continuum consists of millions of peaks equally spaced by the repetition rate of the laser [21]. Indeed, the usage of the SC generated in a PCF in the creation of a stabilized frequency comb provides convenient means to link optical frequency standards together. In addition, the relationship between the repetition rate of the pulses and the comb spacing has provided a link between optical and microwave frequencies. This enables comparison of the performance of Cesium atomic clocks with stabilized lasers. Talking about medical science, the SC has been successfully used in medical imaging techniques like Optical coherence tomography (OCT) which is an optical signal acquisition and processing method, where a clean *bell-shaped* spectral profile is essential because these pulses avoid spurious structures in OCT images [22]. It captures micrometer-resolution, three-dimensional images from within optical scattering media (e.g., biological tissue) by an interferometric technique, typically employing near-infrared light. The use of relatively long wavelength light allows it to penetrate into the scattering medium. Confocal microscopy, another optical technique, typically penetrates less deeply into the sample but with higher resolution [23, 24, 25, 26].

Considering the above information, this work is motivated by the interest on develop methods of spectral handling for OCT applications specifically. These methods are capable of finding the optimal input pulse parameters or the optimal fiber dimensions needed to obtain an output spectra exhibiting multiple simultaneous peaks centered at pre-defined wavelengths using a single laser source, peaks so far obtained only by using multiple laser sources [32, 33]. It is enabled by fiber based illumination [27, 28] in the second near IR window (NIR II), where transparency of the biological tissues increases and scattering decreases [25, 26, 29]. Because of the typical dispersion landscape, sources in the NIR II window may be based on Cherenkov radiation and bright optical solitons arising during SC

generation through the intricate soliton fission effect [30, 31]. With this picture in mind, these methods consist in analytic studies based on dispersive waves generation and by using computational genetic algorithms (GAs) for SSFS optimization. Because a simple change in the involved variables can lead to a significant change in the spectral output, GAs are seen as an adequate optimization tool to obtain optimal parameters. All the work is supported by numerical simulations by codes written on Matlab software. The simultaneous presence of the operating spectral components can be used for real time imaging [34, 35]. The peaks we obtain are dispersive waves and Raman solitons presenting a clean *bell-shaped* spectral profile, essential for OCT [23], with widths providing a decent longitudinal resolution $l_c \approx 10$ μm [28]. The use of GAs generally requires a large amount of simulations. For this reason we used the distributed computing (GRID) platform property of the Universitat Politècnica de València (Spain) to reduce the time required to find the optimal solutions. The advantage of this infrastructure is that it enables the use of the same code in a platform of scalable resources which are adapted according to the needs of the particular problem.

This work is organized as follows. In Chapter 2, it is provided a physical model of the nonlinear pulse propagation and a brief description about the main nonlinear effects involved in the SC generation. The Fourier Split-step numerical technique, useful to solve the NLSE, and a detailed description of the used genetic algorithms (GAs) are presented. In Chapter 3, an understanding of how different effects act individually for the spectral broadening under the femtosecond regime is explained. It is shown, in chapter 4, a method to design a non-uniform standard single mode fiber to generate spectral broadening in the form of "ad-hoc" chosen simultaneous *bell-shaped* peaks from dispersive waves. The controlled multi-peak generation is possible by an on/off switch of Cherenkov radiation, achieved by tailoring the fiber dispersion when decreasing the cladding diameter by segments.

In chapter 5, it is shown a method that consists in obtaining firstly a single peak frequency convertor and then a dual-pulse light source exhibiting two predefined simultaneous spectral peaks based on SSFS. They are obtained by optimization of the input pulse parameters. This resulting spectral broadening has a maximum spectral conversion for one or two simultaneous selected channels in the anomalous region just by adjusting the three realistic controllable laser

parameters. The optimizations are performed using a GA designed to detect configurations maximizing the soliton Raman shift in the SC spectral output.

In chapter 6, in order to prove the functionality of our method to obtain a variety of spectral shapes, we obtain an ultra-flat spectrum centred in 1285 nm based on self-phase modulation broadening. Here it is reported a spectrum exhibiting a 1-dB bandwidth of 90 nm and a 0.5-dB bandwidth of 50 nm, taking advantage mainly of spectral broadening of pulses by the self-phase modulation and self-steepening effects. The ultra-flat spectrum can be applied both, for OCT and telecommunication applications.

Finally, in Chapter 7, it is summarized the results and further work for this project.

References

[1] R. R. Alfano and S. L. Shapiro, *"Emission in the region 4000 to 7000 Å via four-photon coupling in glass,"* Phys. Rev. Lett. **24**, 584-587 (1970). 1

[2] P. Nelson, D. Cotter, K. J. Blow, and N. J. Doran, *"Large nonlinear pulse broadening in long lengths of monomode fiber,"* Opt. Commun. **48**, 292-294 (1983). 1

[3] P. L. Baldeck and R. R. Alfano, *"Intensity effects on the stimulated four photon spectra generated by picosecond pulses in optical fibers,"* J. Lightwave Technol. **5**, 1712-1715 (1987). 1, 2

[4] S. Coen, A. H. Lun Chau, R. Leonhardt, J. D. Harvey, J. C. Knight, W. J. Wadsworth, and P. St. J. Russell, *"Supercontinuum generation by stimulated Raman scattering and parametric four-wave mixing in photonic crystal fibers,"* J. Opt. Soc. Am. B **19**, 753-764 (2002). 1, 2

[5] J. M. Dudley, L. Provino, N. Grossard, H. Maillotte, R. S. Windeler, B. J. Eggleton, and S. Coen, *"Supercontinuum generation in air–silica microstructured fibers with nanosecond and femtosecond pulse pumping,"* J. Opt. Soc. Am. B **19**, 765-771 (2002). 1, 2

[6] J. Herrmann, U. Griebner, N. Zhavoronkov, A. Husakou, D. Nickel, J. C. Knight, W. J. Wadsworth, P. St. J. Russell, and G. Korn, *"Experimental Evidence for Supercontinuum Generation by Fission of Higher-Order Solitons in Photonic Fibers,"* Phys. Rev. Lett. **88**, 173901 (2002). 1

REFERENCES

[7] A. V. Husakou, and J. Herrmann, *"Supercontinuum generation of higher-order solitons by fission in photonic crystal fibers,"* Phys. Rev. Lett. **87**, 203901 (2001). 1

[8] C. Lin and R. H. Stolen, *"New nanosecond continuum for excited-state spectroscopy,"* Appl. Phys. Lett. **28**, 216–218 (1976). 2

[9] R. H. Stolen, C. Lee, and R. K. Jain, *"Development of the stimulated Raman spectrum in single-mode silica fibers,"* J. Opt. Soc. Am. **1**, 652–657. (1984). 2

[10] I. Ilev, H. Kumagai, K. Toyoda, and I. Koprinkov, *"Highly efficient wideband continuum generation in a single mode optical fiber by powerful broadband laser pumping,"* Appl. Opt. **35**, 2548–2553. (1996). 2

[11] J. K. Ranka, R. S. Windeler, and A. J. Stentz, *"Visible continuum generation in air-silica microstructure optical fibers with anomalous dispersion at 800 nm,"* Opt. Lett. **25**, 25-27 (2000). 2

[12] D. Mogilevtsev, T. A. Birks, and P. St. J. Russell, *"Nonlinearity in holey optical fibers: Measurement and future opportunities,"* Opt. Lett. **23**, 1662–1664 (1998). 2

[13] N. G. R. Broderick, T. M. Monro, P. J. Bennett, and D. J. Richardson, *""Group-velocity dispersion in photonic crystal fibers,"* Opt. Lett. **24**, 1395–1397 (1999). 2

[14] C. Milián, A. Ferrando, and D. V. Skryabin, "Polychromatic Cherenkov radiation and supercontinuum in tapered optical fibers," J. Opt. Soc. Am. B **29,** 589-593 (2012). 2

[15] X. Liu, C. Xu, W. H. Knox, J. K. Chandalia, B. J. Eggleton, S. G. Kosinski, and R. S. Windeler, "Soliton self-frequency shift in a short tapered air–silica microstructure fiber," Opt. Lett. **26,** 358-360 (2001). 2

[16] F. Parmigiani, C. Finot, K. Mukasa, M. Ibsen, M. A. F. Roelens, P. Petropoulos, and D. J. Richardson, "Ultra-flat SPM-broadened spectra in a highly nonlinear fiber using parabolic pulses formed in a fiber Bragg grating," Opt. Express **14,** 7617-7622 (2006). 2

[17] T. Morioka, H. Takara, S. Kawanishi, O. Kamatani, K. Takiguchi, K. Uchiyama, M. Saruwatari, H. Takahashi, M. Yamada, T. Kanamori and, H. Ono, *"1 Tbit / s (100 Gbit / sx10 channel) OTDM / WDM transmission using a single supercontinuum WDM source,"* Electron. Lett. **32**, 906-907 (1996). 3

[18] S. T. Cundiff, J. Ye and, J. L. Hall, *"Optical frequency synthesis based on mode locked lasers,"* Rev. Sci. Instrum **72**, 3749-3771 (2001). 3

[19] H. Takara, T. Ohara, K. Mori, K. Sato, E. Yamada, Y. Inoue, *"More than 1000 channel optical frequency chain generation from single supercontinuum source with 12.5 GHz channel spacing,"* Electron. Lett. **36**, 2089-2090 (2000). 3

[20] K. Mori, T. Morioka and, M. Saruwatari, *"Ultrawide spectral range group-velocity dispersion measurement utilizing supercontinuum in an optical fiber pumped by a 1.5 μm compact laser source,"* IEEE Trans. Instrum. Meas. **44**, 712-715 (1995). 3

[21] S. A. Diddams, D. J. Jones, J. Ye, S. T. Cundiff and, J. L. Hall, *"Direct Link between Microwave and Optical Frequencies with a 300 THz Femtosecond Laser Comb,"* Phys. Rev. Lett. **84**, 5102 (2000). 3

[22] R. Tripathi, N. Nassif, J. S. Nelson, B. H. Park, and J. F. de Boer, *"Spectral shaping for non-Gaussian source spectra in optical coherence tomography,"* Opt. Lett. **27**, 406–408 (2002). 3

[23] J.G. Fujimoto, C. Pitris, S. A. Boppart, and M.E, Brezinski, *"Optical coherence tomography: An emerging technology for biomedical imaging and optical biopsy,"* Neoplasia **2,** 9-25 (2000). 3, 4

REFERENCES

[24] P. Cimalla, J. Walther, M. Mehner, M. Cuevas, and E. Koch, *"Simultaneous dual-band optical coherence tomography in the spectral domain for high resolution in vivo imaging,"* Opt. Express **17,** 19486-19500 (2009). 3

[25] A.M Smith, M.C. Mancini, and S. Nie, *"Bioimaging: Second window for in vivo imaging,"* Nat. Nanotechnol. **9,** 1748-3387 (2009). 3

[26] Q. Cao, N.G. Zhegalova, S.T. Wang, W.J. Akers, and M.Y. Berezin, *"Multispectral imaging in the extended near-infrared window based on endogenous chromophores,"* J. Biomed. Opt. **18,** 101318-101318 (2013). 3

[27] Y. Wang, Y. Zhao, J. S. Nelson, Z. Chen, R. S. Windeler, "Ultrahigh-resolution optical coherence tomography by broadband continuum generation from a photonic crystal fiber," Opt. Lett. **28,** 182–184 (2003). 3

[28] F. Spoeler, S. Kray, P. Grychtol, B. Hermes, J. Bornemann, M. Foerst and H. Kurz, "Simultaneous dual-band ultra-high resolution optical coherence tomography," Opt. Express **15,** 10832-10841 (2007). 3

[29] J.M. Huntley, T. Widjanarko, and P.D. Ruiz, "Hyperspectral interferometry for single-shot absolute measurement of two-dimensional optical path distributions," Meas. Sci. Technol. **21,** 075304 (2010). 3

[30] Y. Kodama and A. Hasegawa, "Nonlinear Pulse Propagation in a Monomode Dielectric Guide," IEEE J. Quantum Elect. **23,** 510-524 (1987). 4

[31] R. Driben, B. A. Malomed, A. V. Yulin and D. V. Skryabin, "Newton's cradles in optics: From N-soliton fission to soliton chains," Phys. Rev. A **87,** 063808 (2013). 4

[32] J.N. Farmer and C.I. Miyake, *"Method and apparatus for optical coherence tomography with a multispectral laser source,"* U.S. Patent 6,538,817 filed October 17, 2000, and issued March 25, 2003. 3

[33] J.M. Huntley, P.D, Ruiz, and T. Widjanarko, *"Apparatus for the absolute measurement of two dimensional optical path distributions using interferometry,"* U.S. Patent 2,011,010,092 filed July 20, 2010, and issued July 12, 2012. 3

[34] F. I. Feldchtein, G. V. Gelikonov, V. M. Gelikonov, R. R. Iksanov, R. V. Kuranov, A. M. Sergeev, N. D. Gladkova, M. N. Ourutina, J. A.Warren, and D. H. Reitze, *"In vivo OCT imaging of hard and soft tissue of the oral cavity,"* Opt. Express **3,** 239-250 (1998). 4

[35] V. M. Gelikonov, G. V. Gelikonov, and F. I. Feldchtein, *"Two-wavelength optical coherence tomography,"* Radiophys. Quantum Electron. **47,** 848?859 (2004). 4

REFERENCES

2

Supercontinuum modelling and the genetic algorithms

The propagation of an electromagnetic wave or a pulse depends on the propagation medium. The pulse propagates unchanged in vacuum, however, the electromagnetic field interacts with the atoms in a medium when it is propagating which leads to experiment losses and dispersion. Dispersion occurs because different spectral components of the pulse travels at different velocities due to the dependence of refractive index (n) on wavelength (λ) (see. Section 3.5). In an optical waveguide, the dispersion has an additional contribution due to light confinement. It is known as waveguide dispersion, which can not be suppressed because of a frequency-dependent distribution of wave vectors (k vectors) in a guided wave. Moreover, if the field intensity is enough high, the medium has a nonlinear response. Most notably, the refractive index becomes intensity dependent (*Kerr effect*) and photons interact with phonons of the medium (Raman effect) [1]. Electromagnetic wave propagation in optical fibers is governed by the generalized nonlinear Schrödinger equation (GNLSE) and, an efficient tool to optimize the spectral output of the GNLSE are genetic algorithms (GAs). A genetic algorithm (GA) is an optimization technique for searching very large spaces that models the role of the genetic material in living organisms. Computational techniques that emulate these optimization process has been developed in order to optimize complex systems where many parameters are involved. Pulse parameters and fiber dimensions are optimized using GAs in this work. A small

population of individual exemplars can effectively search for a large space because they contain schemata, useful substructures that can be potentially combined to make fitter individuals. Formal studies of competing schemata show that the best policy for replicating them is to increase them exponentially according to their relative fitness. This turns out to be the policy used by GAs. Fitness is determined by examining a large number of individual fitness cases. This process can be very efficient if the fitness cases also evolve by their own GA.

This chapter provides a physical model of the nonlinear pulse propagation and a brief description about the main nonlinear effects playing an important role in the SC generation when an electric field is propagated in an optical fiber. Then, the Fourier split-step numerical technique useful to solve the NLSE. Finally, a detailed description of the used GA are presented to completing the optimization tools used in this work.

2.1 Nonlinear pulse propagation

To modelling the nonlinear pulse propagation in optical fibers is necessary to include the nonlinear polarization of the medium in Maxwell's equations and derive a second-order wave equation which is approximated to a first order propagation equation for the pulse [2, 3]. It is considered only a scalar treatment here.

In the first place, it is necessary to define the electric field (linearly polarized along $\mathbf{x}$) as: $\mathbf{E}(\mathbf{r},t) = \frac{1}{2}\mathbf{x}\{E(x,y,z,t)\exp^{-i\omega_0 t} + c.c\}$. In the frequency domain, the Fourier transform of $E(x,y,z,t)$ is: $\tilde{E}(x,y,z,\omega) = F(x,y,\omega)\tilde{A}(z,\omega - \omega_0)\exp^{i\beta_0 z}$ where $\tilde{A}(z,\omega)$ is the complex spectral envelope, while ω_0 is a reference frequency and β_0 is the wave number at that frequency. $F(x,y,\omega)$ is the transverse modal distribution.

The time-domain envelope is obtained as

$$A(z,t) = \mathcal{F}^{-1}\{\tilde{A}(z,\omega-\omega_0)\} = \frac{1}{2\pi}\int_{-\infty}^{\infty}\tilde{A}(z,\omega-\omega_0)\exp[-i(\omega-\omega_0)t]d\omega, \quad (2.1)$$

where the amplitude is normalized such that $|A(z,t)|^2$ gives the instantaneous power and $\mathcal{F}^{-1}$ denotes the inverse Fourier transform. Using this notation implementing the change of variable $T = t - \beta_1 z$ to transform into a co-moving frame

at the envelope group velocity β_1^{-1}, we obtain a time-domain generalized NLSE for the evolution of $A(z,T)$:

$$\begin{aligned} \frac{\partial A}{\partial z} &+ \frac{\alpha}{2}A - \sum_{k\geq 2}\frac{i^{k+1}}{k!}\beta_k\frac{\partial^k A}{\partial T^k} \\ &= i\gamma(1+i\tau_{shock}\frac{\partial}{\partial T})(A(z,T)\int_{-\infty}^{\infty}R(T')|A(z,T-T')|^2dT'). \end{aligned} \quad (2.2)$$

The left-hand side of this equation models linear propagation effects, with α being the linear power attenuation and β_k are the dispersion coefficients associated with the Taylor series expansion of the propagation constant $\beta(\omega)$ around ω_0 (see Section 3.5). The right-side of the equation models the nonlinear effects, where

$$\gamma = \frac{\omega_0 n_2(\omega_0)}{cA_{eff}(\omega_0)} \quad (2.3)$$

is the nonlinear coefficient, $n_2(\omega_0)$ is the nonlinear refractive coefficient and $A_{eff}(\omega_0)$ is the effective modal area, both of them are evaluated at ω_0. The Raman response function is $R(T) \equiv [1-f_R]\delta(T) + f_R h_R(T)\Pi(T)$, where $f_R = 0.18$ is the fractional contribution of the Raman response (see Section 3.6), h_R is the commonly used Raman response of silica [4], and $\delta(T)$ and $\Pi(T)$ are the Dirac and Heaviside functions, respectively. The input pulses in our modeling are taken as

$$A(z=0,T) \equiv \sqrt{P_0}\,\mathrm{sech}(T/T_0) \quad (2.4)$$

with $T_0 \equiv T(z=0) \equiv T_{FWHM}/2\ln[1+\sqrt{2}]$, where T_{FWHM} is the full width at half maximum. With these parameters, the soliton order is given as

$$N \equiv T_0\sqrt{\frac{\gamma P_0}{|\beta_2|}}. \quad (2.5)$$

The time derivative term on the right-hand side of Eq. 2.2 models the dispersion of the nonlinearity such as self-steepening and optical shock formation, characterized by a time scale $\tau_{shock} = \tau_0 = 1/\omega_0$. Additional dispersion arises

from the frequency dependence of the effective area, and τ_{shock} can be generalised to account for this in an approximate manner [2].

2.1.1 Fourier split-step numerical solution

The greater relative speed of this method compared with most finite difference methods can be attributed in part to the use of the finite-Fourier-transform (FFT) algorithm. Although finite difference methods are more accurate than split-step fourier method, the numerical conditions used in this work make that the relative error can be neglected. To understand the split-step Fourier method, it is useful to write Eq. 2.2 formally in the form

$$\frac{\partial U}{\partial \xi} = \left(\widehat{D} + \widehat{N}\right) U \tag{2.6}$$

where $U = A/\sqrt{P_0}$ is the normalized amplitude, $\xi = z/L_D$ is the normalized distance using the L_D scale, $\widehat{D}$ is a differential operator that accounts for dispersion in a linear medium and $\widehat{N}$ is a nonlinear operator that governs the nonlinear effect on pulse propagation [4]. These operators are given by

$$\widehat{D} = \sum_{k\geq 2}^{\infty} \frac{-(i^{k-1})}{k!} \beta_k \frac{\partial^k}{\partial T^k} - \frac{\alpha}{2} \tag{2.7}$$

$$\widehat{N} = i\gamma \left(|A|^2 + \frac{2i}{\omega_0 A} \frac{\partial}{\partial T} \left(|A|^2 A \right) - T_R \frac{\partial |A|^2}{\partial T} \right). \tag{2.8}$$

In general, dispersion and nonlinearity act together along the length of the fiber. The split-step Fourier method obtains an approximate solution by assuming that in propagating the optical field over a small distance h, the dispersive and nonlinear effects can be considered to act independently. More specifically, propagation from ξ to $\xi + h$ is carried out in two steps. In the first step, nonlinearity acts alone, and $\widehat{D} = 0$, in Eq. 2.6. In the second step, dispersion acts alone, and $\widehat{N} = 0$. Both the linear and the nonlinear parts have analytical solutions, but the nonlinear Schrödinger equation containing both parts does not have a general analytical solution. Mathematically

$$U\left(\xi + h, T\right) = \exp(h\widehat{D}) \exp(h\widehat{N}) U\left(\xi, T\right). \tag{2.9}$$

The execution of the exponential operator $\exp(h\widehat{D})$ is carried out in the Fourier domain using the prescription

$$\exp(h\widehat{D})U(\xi,T) = \left\{\mathcal{F}^{-1}\exp\left[h\widehat{D}(i\omega)\right]\mathcal{F}\right\}U(\xi,T) \tag{2.10}$$

where $\mathcal{F}$ denotes Fourier transform operation and ω is the frequency. Since $\widehat{D}(i\omega)$ is just a number in the Fourier space, the evaluation of Eq. 2.10 is straightforward. The use of the FFT algorithm makes the numerical evaluation of Eq. 2.10 relatively fast. It is for this reason that the split-step Fourier method can be faster by up to two orders of magnitude compared with most finite difference schemes.

To estimate the accuracy of the split-step Fourier method, we note that a formally exact solution of Eq. 2.6 is given by

$$U(\xi+h,T) = \exp\left[h(\widehat{D}+\widehat{N})\right]U(\xi,T), \tag{2.11}$$

using Baker-Hausdorff theorem we can see the solution [5]

$$U(\xi+h,T) = \exp\left(h(\widehat{D})\right)\exp\left(h(\widehat{N})\right)U(\xi,T), \tag{2.12}$$

which is a quick and simple equation for numerical analysis of pulse propagation in dispersive and nonlinear media.

2.2 Genetic algorithms and GRID platform

The GA associates the genome $\mid g\rangle \equiv [g_1, g_2, g_3]^T$, with the spectral output of each pulse propagation simulation characterizing each *individual* of the population, and applies a minimization strategy to find the solutions taking the minimum values of a fitness function.

Because exhaustive enumeration of the search space is in general impractical, the GA (meta-heuristic algorithms) accepts solutions which approximate to a global optima, but may not exactly match it, what provides shorter runtime. Here the genetic operators responsible for the population evolution towards to the minimum fitness value ϕ_{min} are mainly the identity operator $\hat{I}$, random generation $\hat{\mathcal{R}}$, mutation $\hat{\mathcal{M}}$ and crossover $\hat{\mathcal{X}}$.

2. SUPERCONTINUUM MODELLING AND THE GENETIC ALGORITHMS

Random generation is regarded as

$$\hat{\mathcal{R}} \mid \phi\rangle \equiv \begin{bmatrix} R_1 & 0 & 0 \\ 0 & R_2 & 0 \\ 0 & 0 & R_3 \end{bmatrix} \mid \phi\rangle \rightarrow \mid g\rangle, \tag{2.13}$$

where R_k are the random generators (creators) obeying a uniform statistical distribution and $\mid \phi\rangle$ is the zero or *vacuum* state. The mutation $\hat{\mathcal{M}} :\mid g\rangle \rightarrow \mid g'\rangle$ uses polynomial mutation [6] for real coded problems (continuous valued variables), and generates the new genes as

$$g'_k = g_k + m_k \Delta_k \bar{\zeta}_k;\ m_k \equiv \Theta(u_k - \frac{2}{3}), \tag{2.14}$$

where Δ_k is half of the allowed interval for each variable, Θ is the Heaviside step function and $u_k \in [0,1]$ a uniform random number, so in average, only one gene is mutated per individual when mutation is applied. $\bar{\zeta}_k \in [-1,1]$ satisfies the normalized probability distribution $\mathcal{P}_m(\zeta) = 0.5[n+1[1-|\zeta|]^n]$ with the factor of probability distribution $n = 20$ (see fig. 2.1a). $\mathcal{P}$ becomes the normal distribution for $n = 0$ or it is very peaked around zero for $n \gg 1$, so it is clearly distinguished from R_k. The stochastic variable is chosen via a new random $u_k \in [0,1]$ as

$$\bar{\zeta}_k = \zeta \mid \int_{-1}^{\zeta} \mathcal{P}_m(\zeta) d\zeta = u_k;\ u_k \in [0,1]. \tag{2.15}$$

Cross-over generates two *childs* $\mid g_c^{1,2}\rangle$ by combining two *parents*, $\mid g_p^{1,2}\rangle$, without destroying the last, i.e., $\hat{\mathcal{X}}[\mid g_p^1\rangle^T, \mid g_p^2\rangle^T, \mid \phi\rangle^T, \mid \phi\rangle^T]^T = [\mid g_p^1\rangle^T, \mid g_p^2\rangle^T, \mid g_c^1\rangle^T, \mid g_c^2\rangle^T]^T$. We have used SBX (Simulated Binary Crossover) [7] and the $[12 \times 12]$ operator

$$\hat{\mathcal{X}} \equiv \begin{bmatrix} \hat{I} & \hat{0} & \hat{0} & \hat{0} \\ \hat{0} & \hat{I} & \hat{0} & \hat{0} \\ \hat{\alpha}_+ & \hat{\alpha}_- & \hat{0} & \hat{0} \\ \hat{\alpha}_- & \hat{\alpha}_+ & \hat{0} & \hat{0} \end{bmatrix};\ (\hat{\alpha}_\pm)_{jk} \equiv x_k \frac{1 \pm \bar{\sigma}_k}{2} \zeta_{jk},;\ x_k \equiv \Theta(u_k - 0.05), \tag{2.16}$$

where $\hat{0} \equiv 0 \times \hat{I}$. . The crossover *activators*, x_k, set a probability for cross over of 95% per gene (note $(\hat{\alpha}_\pm)_{jk}$ preserve the average value of each parameter under

crossover, $|g^2_{pk} - g^1_{pk}| = |g^2_{ck} - g^1_{ck}|$). The stochastic variables in this case, $\bar{\sigma}_k$ (see fig. 2.1b), are again chosen from $u_k \in [0, 1]$,

$$\bar{\sigma}_k = \sigma \int_0^{\sigma} \mathcal{P}_x(\sigma) d\sigma = u_k; \; \mathcal{P}_x(\sigma) = \begin{cases} 0.5(n+1)\sigma^n, \; \sigma \leq 1 \\ 0.5(n+1)\sigma^{-(n+2)}, \; \sigma > 1 \end{cases} . \tag{2.17}$$

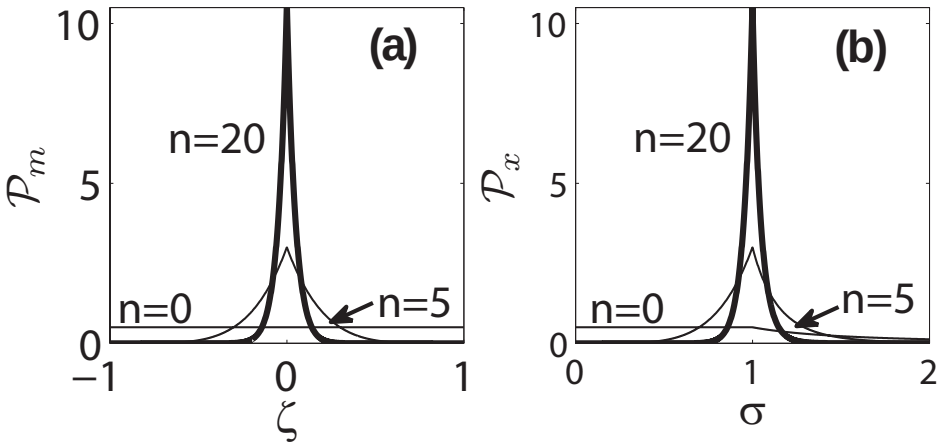

Figure 2.1: Probability distributions for the stochastic variables involved in (a) polynomial mutation and simulated binary crossover in (b).

Most of traditional GA are *generational*, i.e., start from a randomly generated population and the most promising individuals are allowed to reproduce to determine the next generation of individuals, according to the pre-established evolution rules (parent selection method, definition of $\hat{\mathcal{M}}$, $\hat{\mathcal{X}}$ and their rates, to obtain the offspring for the next generation). Most parent selection methods are stochastic in order to keep the diversity of the population, preventing premature convergence to a sub-optimal solution. A steady state GA has been used, changing one member of the population at a time. This allows computation of several fitness in parallel (after an initial population p has been built) and processed once they are available. To this end, a *replace the worst* strategy has been adopted, which fully exploits the processing power of a Grid platform, keeping it constantly computing new individuals. The algorithm decides what to do with the generated individuals in the first stage and in the second stage how to make

the new ones. In the former, a newly generated individual is added to the population (regardless its ϕ) if the size is less than p. If the current population is already p, the new candidate replaces the individual with the worst (biggest) ϕ if any, or it is discarded. The second stage is to generate new individuals to be sent to the Grid for evaluation. This is done by $\hat{\mathcal{R}}$ if population is smaller than the threshold value c ($c < p$), or by the genetic operators $\hat{\mathcal{M}}$ and $\hat{\mathcal{X}}$ otherwise. Whilst $\hat{\mathcal{M}}$ provides diversity to the population, $\hat{\mathcal{X}}$ pulls the new individuals closer to the currently lowest Φ. *Generation* is thus a not well defined concept of our scheme, since an individual survival is guaranteed until it becomes the worst one (higher fitness value) in the population. In that sense, the identity operator $\hat{I}$ is always present in the system and only mutation and cross-over are explicitly applied to generate off-springs.

It is convenient to establish a distinction between two different categories of parameters that can be optimized: external and structural. External parameters are those whose characteristics can be modified in real time, the properties of the pump pulse can be included in this category: e.g., its temporal width (T_0), wavelength (λ_0), power peak (P_0), chirp (C), polarization (P), etc. On the contrary, structural parameters can not be changed once established unless the medium is physically modified. These are, for example, all the non-tunable fabrication parameters of the optical fiber as well as other further fiber modifications such as taper profiles, Bragg or long period gratings, etc.

Since it is wanted to tailor the spectral output by searching the adequate fiber properties, the objective is to manipulate only the fiber parameters in chapters 4 and 6. On the other hand, the laser characteristics are only manipulated as external parameters to optimize the Raman conversion through SC generation in chapter 5. Every set of input pulse parameters along with their corresponding *fitness* function constitutes an individual. In order to clarify the exposition, we provide a descriptive chart of the algorithm in fig.2.2.

At stage one, the algorithm generates a random population by evaluating the output spectra of p randomly selected individuals (i.e., p different sets of input pulse parameters) using Eq.(2.2) and evaluating their corresponding *fitness* function. At stage two, the GA starts to act properly by generating new individuals using genetic operators successively. The population dimension is always kept

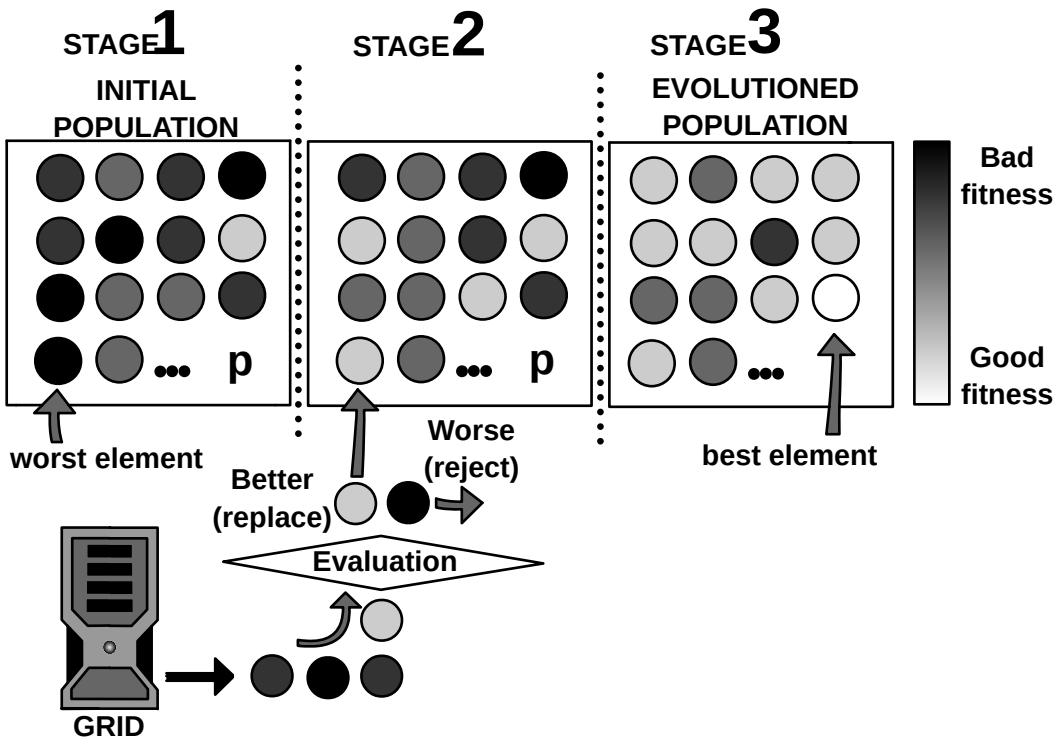

Figure 2.2: General diagram of the operation of the GA using a GRID platform. The process causes the mean fitness improvement in the population. After m executions, the best individual is picked from the evolved population and chosen as optimal solution.

equal to p. In general terms, the GA substitutes the worst individual of the population (largest fitness value) by a better one (with lower fitness value) in each new generation. More specifically, the computational platform (in our case, the Grid) generates new individuals, as many as the computational infrastructure permits, by running Eq.(2.2) using new sets of input external parameters, each set defining a new individual. These new sets of parameters are determined by the action of genetic operators on the set of parameters of the population of the previous generation. Roughly speaking, genetic operators mix the parameters of the best individuals contained in the previous generation (parent selection). Most parent selection methods are stochastic in order to keep the diversity of the population, preventing premature convergence to a sub-optimal solution. Each new computed individual is compared against all members of the population of

the previous generation. Only if the new individual presents a better fitness value than that of the worst element of the previous generation, it is accepted. Thus, a new generation with a better average fitness is created. This process is repeated $m - p$ times, so that the total number of executions is m. The value of the total number of executions m is selected in function of the convergence behavior of the GA. At the three and final stage of the process, the best individual of the final population with the lowest fitness is selected as the optimum. This individual is, by construction, the most evolved one and the parameters which characterize it are selected as the optimal ones.

The amount of combinations of parameters evaluated has an important impact on the ability of the GA to find an optimum solution. The time-machine cost exceeds the computational capabilities of a single machine, this is one of the reasons why the deployment of the GA is performed using distributed computing in the form of a Grid platform. Moreover our optimization problem with a potentially very high throughput can be efficiently addressed in an inherently scalable platform as the Grid. For our particular optimization problems, we have used, although we are not restricted to, an integrated computational approach in the form of a cluster of PC's within a Grid infrastructure. The usage of Grid protocols to support these executions makes possible to provide the GA with a scalable solution for more demanding computational necessities. If due to optimization requirements, for example, by increasing the dimension of the search space, additional computational resources are required, the Grid infrastructure can be transparently enlarged by adding new networked computational facilities (computer clusters, supercomputers, etc). Our particular scheme of the Grid is provided by a simple arrangement of a number of PC's machines (50 in our case) controlled by a master computer. The purpose of the Grid is to take advantage of the large quantity of accessible processors in order to execute as many simulations as possible simultaneously. This feature results in a much faster an efficient use of the GA reducing considerably the overall optimization time.

References

[1] J. M. Dudley and J. R. Taylor, *"Supercontinuum generation in optical fibers,"* (Cambridge, 2010). 13

[2] K. J. Blow and D. Wood, *"Theoretical description of transient stimulated Raman scattering in optical fibers,"* IEEE J. Quant. Electron. **25**, 2665-2673 (1989). 14, 16

[3] J. Laegsgaard, *"Mode profile dispersion in generalised nonlinear Schrödinger equation,"* Opt. Express **15**, 16110-16123 (2007). 14

[4] G. P. Agrawal, *Nonlinear Fiber Optics, 4th ed.* (Academic Press. 2007). 15, 16

[5] Y. Bashkatov, B. Tsyganok, V. Khomenko, N. Kachalova, V. Voitsekhovich, and I. Uvarova, *"Modeling supercontinuum generation in microstructured fibers by femtosecond pump pulses using Split-Step Fourier method,"* Electronics Technology (ISSE), 2012 35th International Spring Seminar. 9-13 May (2012). 17

[6] K. Deb,, *Multi-Objective Optimization using Evolutionary Algorithms* (Wiley & Sons, 2001). 18

[7] R. B. Agrawal and K. Deb, *Simulated Binary Crossover for Continuous Search Space* (Technical report, 1994). 18

REFERENCES

3

Dynamics of supercontinuum

Supercontinuum (SC) generation involves the interplay between nonlinear and linear effects that can occur during the propagation of an optical field. SC generation is a process where laser light is converted to light with a very broad spectral bandwidth (i.e., low temporal coherence), whereas the spatial coherence mostly remains the same. The spectral broadening is usually accomplished by propagating optical pulses through a strongly nonlinear material like bulk glass. Alternatively, sending pulses with low energy through an optical fiber, it is possible to have a considerably higher nonlinearity and also a waveguide structure which ensures a high beam quality. In some cases, tapered fibers can also be used (see Chapters 4 and 6). Of special interest are photonic crystal fibers (see Chapter5), mainly due to their unusual chromatic dispersion characteristics, which can allow a strong nonlinear interaction over a significant length of fiber.

Even with fairly moderate input powers a very broad spectrum is achieved. The physical processes behind SC generation in fibers can be very different, depending particularly on the chromatic dispersion and length of the fiber (or other nonlinear medium), the pulse duration, T_0, the initial peak power, P_0 and the pump wavelength, λ_0. When femtosecond pulses are used, the spectral broadening can be dominantly caused by self-phase modulation (SPM) in normal dispersion. In the anomalous dispersion regime, the combination of SPM and dispersion can lead to complicated soliton dynamics, including the split-up of higher-order solitons into multiple fundamental solitons (soliton fission). For pumping with picosecond or nanosecond pulses, Raman scattering and four-wave mixing can be

important. SC generation is even possible with continuous-wave beams, when using multi-watt laser beams in long fibers; Raman scattering and four-wave mixing are very important in that regime. In this chapter, an understanding of how different phenomena act individually for the spectral broadening under the femtosecond regime is explained.

3.1 Dispersion

Dispersion arises because the frequency variation of the effective index of the guided mode depends on both material and waveguide contributions (frequency-dependent distribution of wave vectors). Even speaking of a monochromatic pulse, frequencies associated near the central frequency exist, because of this, it is better named quasi-monochromatic pulse. This work takes into account only the chromatic dispersion of the fundamental guide mode. However, more generally, it is also necessary to consider additional dispersion contributions due to polarization mode dispersion in the case of a birefringent fiber or the higher order intermodal dispersion between transverse modes in a multimode fiber.

Optical pulse transmission suffers distortion of pulse shape from chromatic dispersion. This is true, in particular, when the pulse is produced by a partially coherent light with a substantial spectral width. For example, a directly modulated semiconductor laser with multi longitudinal modes brings about a pulse degradation caused by the modal dispersion [1]. Kapron and Keck [2] calculated the distortion of a Gaussian pulse after transmission through a single-mode fiber by monochromatic light. Their result is showed in fig 3.1. Here, the pulse broadening is caused by the fiber dispersion of frequency components inherent in the finite width of the input pulse.

Generally the refractive index decreases as wavelength increases, blue light traveling more slowly in the material than red light. Dispersion is the phenomenon which gives the separation of colors in a prism. It also gives the generally undesirable chromatic aberration in lenses. When an electromagnetic wave interacts with bound electrons of a dielectric, the medium response in general depends of the optical frequency. This property is referred to as chromatic dispersion. On

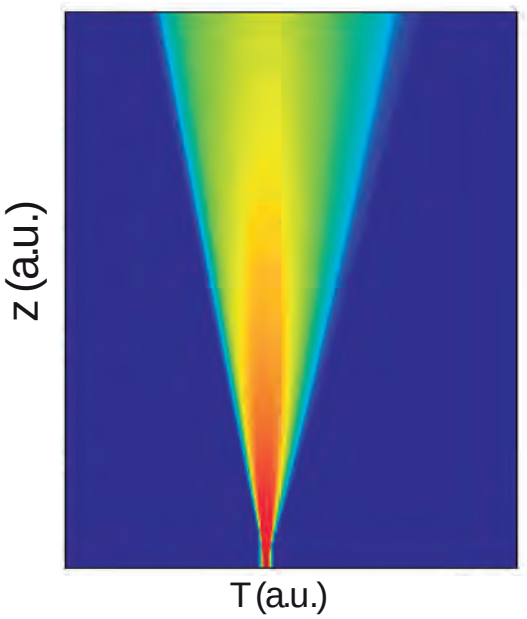

Figure 3.1: Gaussian pulse evolution due to dispersion effect.

a fundamental level, the origin of chromatic dispersion is related to the characteristic resonance frequencies at which the medium absorbs the electromagnetic radiation through oscillations of bound electrons [3].

Far from the medium resonance, the refractive index is approximated by the Sellmeier equation,

$$n^2(\omega) = +\sum_{j=1}^{m} \frac{B_j \omega_j^2}{\omega_j^2 - \omega^2}, \tag{3.1}$$

where ω_j is the resonant frequency and B_j is the strength of the resonance.

Fiber dispersion plays a critical role in propagation of short optical pulses since different spectral components associated with the pulse travel at different speeds given by $c/n(\omega)$. Even when the nonlinear effects are not important, dispersion induced pulse broadening can be detrimental for optical communications systems. In the nonlinear regime, the combination of dispersion and nonlinearity can result in a qualitatively different behavior. Mathematically, the effects of fiber dispersion are accounted for by expanding the mode propagation constant

β in a Taylor series about the central frequency ω_0:

$$\beta(\omega) = n(\omega)\frac{\omega}{c} = \sum_{0}^{n=\infty} \frac{1}{n!}\beta_n(\omega - \omega_0)^n, \tag{3.2}$$

where

$$\beta_m = \left[\frac{d^m\beta}{d\omega^m}\right]_{\omega=\omega_0}; \qquad (m = 0, 1, 2, 3...). \tag{3.3}$$

The pulse envelope moves at the group velocity $V_g = 1/\beta_1$ while the parameter β_2 is responsible for pulse broadening.

3.2 Self-phase modulation

The greater intensity portions of an optical pulse encounter a higher refractive index of the medium compared with the lower intensity portions while it travels through the medium. In fact time varying pulse intensity produces a time varying refractive index in a medium that has an intensity-dependent refractive index. The leading edge will experience a positive refractive index gradient (dn/dt) and trailing edge a negative refractive index gradient (-dn/dt). This temporally varying index change results in a temporally varying phase change. The optical phase changes with time in exactly the same way as the optical signal [4]. Since, this nonlinear phase modulation is self-induced the nonlinear phenomenon responsible for it is called Self-phase modulation (SPM). Different parts of the pulse undergo different phase shift because of intensity dependence of phase fluctuations. This results in frequency chirping. The leading edge of the pulse has a frequency shift in the upper side whereas the trailing edge experiences a frequency shift in the lower side. Hence, the primary effect of SPM is to broaden the spectrum of the pulse [5], keeping the temporal shape unaltered. The SPM effects are more pronounced in systems with high-transmitted power because the chirping effect is proportional to transmitted signal power. The phase (θ) introduced by a field E over a fiber length L is given by

$$\theta = \frac{2\pi}{\lambda}nL \tag{3.4}$$

where λ is wavelength of optical pulse propagating in fiber of refractive index n, and nL is known as optical path length. For a fiber containing high-transmitted power, n and L can be replaced by n_{eff} and L_{eff}, respectively i.e.,

$$\theta = \frac{2\pi}{\lambda} n_{eff} L_{eff} \tag{3.5}$$

or

$$\theta = \frac{2\pi}{\lambda} \left(n_l + n_{nl} I\right) L_{eff}. \tag{3.6}$$

The first term on the right hand side of Eq. 3.6 refers to linear portion of phase constant (θ_l) and second term provides nonlinear phase constant (θ_{nl}). If the intensity is time dependent i.e., the wave is temporally modulated then the phase will also depend on time [6]. This variation in phase with time is responsible for change in frequency of the spectrum, which is given by

$$\omega = \frac{d\theta}{dt}. \tag{3.7}$$

In a dispersive medium a change in the spectrum of temporally varying pulse will change the nature of the variation. To observe this, let's consider a Gaussian pulse, which modulates an optical carrier frequency ω and the instantaneous frequency becomes,

$$\omega' = \omega_0 + \frac{d\theta}{dt}. \tag{3.8}$$

The sign of the phase shift due to SPM is negative because of the minus sign in the phase expression, $(\omega t - kz)$, therefore ω becomes,

$$\omega' = \omega_0 - \frac{2\pi}{\lambda} L_{eff} n_{nl} \frac{dI}{dt}. \tag{3.9}$$

In the leading edge of the pulse, $dI/dt > 0$ hence

$$\omega' = \omega_0 + \omega(t), \tag{3.10}$$

and in the trailing edge $dI/dt < 0$ so,

$$\omega' = \omega_0 - \omega(t). \tag{3.11}$$

where,

$$\omega(t) = \frac{2\pi}{\lambda} L_{eff} n_{nl} \frac{dI}{dt}. \tag{3.12}$$

This shows that the pulse is chirped i.e., it varies on frequency across the pulse. This chirping phenomenon is generated due to SPM, which leads to the spectral broadening of the pulse. There is broadening of the spectrum without any change in temporal distribution in case of SPM, while in case of dispersion, there is broadening of the pulse in the time domain and spectral contents are unaltered. In other words, the SPM by itself leads only to chirping, regardless of the pulse shape. Dispersion is responsible for pulse broadening. The SPM induced chirp modifies the pulse broadening effects of dispersion.

In general, the spectrum not only depends on the pulse shape but also depends on the initial chirp imposed on the pulse. Figure 3.2 shows the spectra of an unchirped Gaussian pulse for several values of the maximum phase shift θ_{max}.

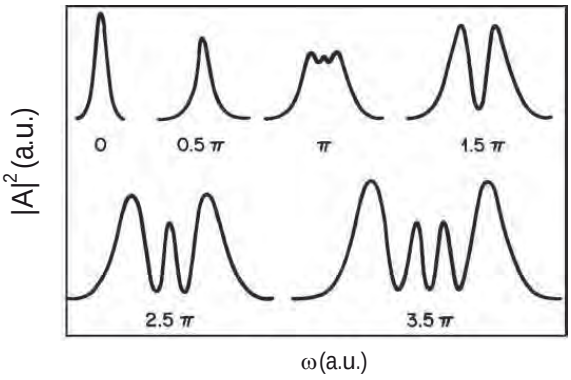

Figure 3.2: SPM-broadened spectra for an Gaussian pulse. Spectra are labeled by the maximum nonlinear phase shift θ_{max} [3].

In solitons, SPM also leads to chirping with lower frequencies in the leading edge and higher frequencies in the trailing edge. On the other hand the chirping caused by linear dispersion, in the wavelength region above zero dispersion wavelength, is associated with higher frequencies in leading edge and lower frequencies in the trailing edge. Both these effects are opposite. By proper choice of pulse shape (a hyperbolic secant-shape) and the power carried by the pulse, one effect can be compensated with the other. In such situation the pulse would

propagate undistorted by mutual compensation of dispersion and SPM. Such a pulse would broaden neither in the time domain (as in linear dispersion) nor in frequency domain (as in SPM) and is called soliton [7, 8]. Since soliton pulse does not broaden during its propagation, it has tremendous potential for applications in super high bandwidth optical communication systems.

3.3 Cross-phase modulation

The SPM is the major nonlinear limitation in a single channel system. The intensity dependence of refractive index leads to another nonlinear phenomenon known as cross-phase modulation (XPM). When two or more optical pulses propagate simultaneously, the cross-phase modulation is always accompanied by SPM and occurs because the nonlinear refractive index seen by an optical beam not only depends on the intensity of that beam but also on the intensity of the other copropagating beams [9]. In fact XPM converts power fluctuations in a particular wavelength channel to phase fluctuations in other copropagating channels. The result of XPM may be an asymmetric spectral broadening and distortion of the pulse shape. The effective refractive index of a nonlinear medium can be expressed in terms of the input power (P) and effective core area (A_{eff}) as,

$$n_{eff} = n_l + n_{nl}\frac{P}{A_{eff}} \tag{3.13}$$

If the first-order perturbation theory is applied to investigate how fiber modes are affected by the nonlinear refractive index, it is found that the mode shape does not change but the propagation constant becomes power dependent.

$$k_{eff} = k_l + k_{nl}P \tag{3.14}$$

where k_l is the linear term of the propagation constant and k_{nl} is the nonlinear propagation constant. The phase shift caused by the nonlinear propagation constant in traveling a distance L_{eff} inside the fiber is given as

$$\theta_{nl} = \int_0^{L_{eff}} (k_{eff} - k_l)dz \tag{3.15}$$

Using Eqs. 3.14-3.15 nonlinear phase shift becomes,

$$\theta_{nl} = k_{nl} P_{in} L_{eff} \tag{3.16}$$

where P_{in} is the input power. When several optical pulses propagate simultaneously the nonlinear phase shift of first channel θ_{nl}^{1} not only depends on the power of that channel but also depends on signal power of other channels. For two channels of power P_1 and P_2, θ_{nl}^{1} can be given as,

$$\theta_{nl}^{1} = k_{eff} L_{eff} \left(P_1 + 2P_2\right) \tag{3.17}$$

For N-channel transmission system, the shift for the $i-th$ channel can be given as [5]

$$\theta_{nl}^{i} = k_{eff} L_{eff} \left(P_i + 2 \sum_{n \neq i}^{N} P_n \right). \tag{3.18}$$

The factor 2 in above equation has its origin in the form of the nonlinear susceptibility [3] and indicates that XPM is twice as effective as SPM for the same amount of power. The first term in above equation gives the contribution of SPM and the second term gives that contribution of XPM. It can be observed that XPM is effective only when the interacting signals superimpose in time. XPM hinders the system performance through the same mechanisms as SPM: chirp frequency and chromatic dispersion, but XPM can damage the system performance even more than SPM. XPM influences the system severely when number of channels is large.

3.4 Soliton fission

Supercontinuum generation with anomalous GVD regime pumping is dominated by soliton-related propagation effects. The most important of these, in the initial stages, is the soliton fission process, whereby a pulse with sufficient peak power to constitute a higher-order soliton is perturbed and breaks up into a series of

lower-amplitude subpulses. The soliton order of the input pulse, N, is determined by both pulse and fiber parameters through the expression

$$N = \frac{L_D}{L_{nl}}, \tag{3.19}$$

where $L_D = T_0^2/|\beta_2|$ and $L_{nl} = 1/\gamma P_0$ are the characteristic dispersive and nonlinear length scales, respectively.

In the femtosecond regime, higher-order dispersion and Raman scattering are the two most significant effects that can perturb the ideal periodic evolution of the soliton and induce pulse breakup through soliton fission. Which of the two effects dominates depends primarily on the input pulse duration. For input pulses of durations exceeding 200 fs, the input pulse bandwidth is sufficiently low that the Raman perturbation generally dominates, whereas for pulses of duration less than 20 fs, it is the dispersive perturbation that induces the pulse breakup.

Each resultant pulse of the breakup is a constituent of the fundamental soliton and the number of pulses is equal to the incident pulse soliton order. The individual solitons are ejected from the input pulse in an ordered fashion one by one. The ejected solitons are arranged by peak power with the highest peak power solitons exhibiting the largest wavelength relative to the frequency pump.

Explicit expressions for the constituent fundamental soliton amplitude A_j in terms of the parameters of the injected N-order soliton have been obtained theoretically by Kodama and Hasegawa [10] as

$$A_j(z,T) = \sqrt{P_j}\,\mathrm{sech}(\frac{T}{T_j}) \qquad j = 1, ..., N, \tag{3.20}$$

where $P_j = P_0(2N - 2j + 1)^2$ and $T_j = T_0/(2N - 2j + 1)$ are the peak power and temporal width, respectively. Solitons that are ejected earlier have higher amplitudes, shorter durations, and propagate with faster group velocities.

The distance at which fission occurs generally corresponds to the point at which the injected higher-order soliton attains its maximum bandwidth. A number of empirical expressions for this characteristic distance have been obtained in the context of soliton-effect compression [11, 12], but for our purposes we have found that this fission distance can be usefully defined as $L_{fiss} \sim L_D/N$. It is shon in fig. 3.3.

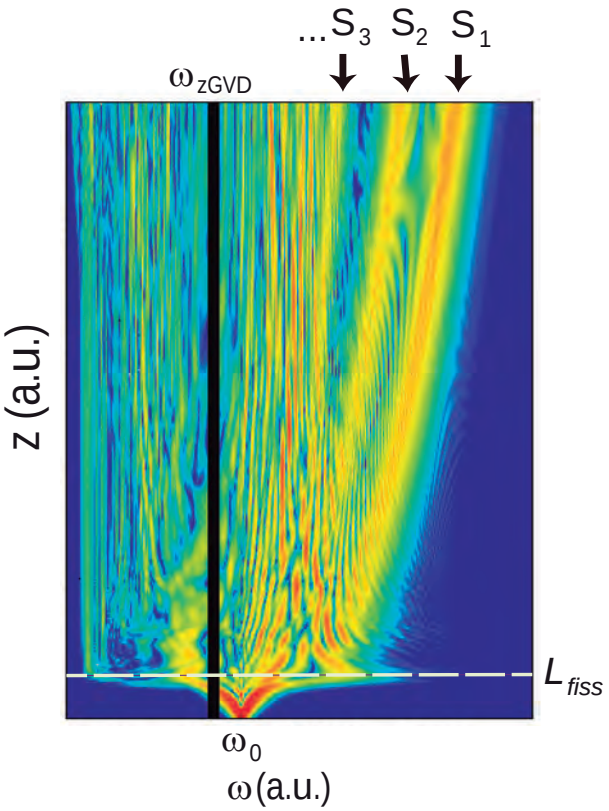

Figure 3.3: Evolution in a uniform SMF showing the soliton fission process, where solitons S_j are ejected after $z = L_{fiss}$. The black line represents the frequency associated to the zero group velocity dispersion (zGVD) wavelength.

3.5 Dispersive waves

The presence of higher-order dispersion can also lead to the transfer of energy from the soliton to a narrow-band resonance in the normal GVD regime, and the associated development of a low amplitude temporal pedestal [13]. The position of this resonance can be readily obtained from a phase-matching argument involving the soliton linear and nonlinear phase and the linear phase of a continuous wave at a different frequency [14, 15, 16].

Fundamental solitons, although robust as they propagate in general, are susceptible to perturbations such as higher order dispersion and the resultant instability manifests as a nonsolitonic radiation (NSR) at a particular frequency [17]. Essentially, a resonance condition involving higher-order dispersion terms comes

into play and leads to a coherent enhancement of the NSR at a narrow band of frequencies as predicted by the appropriate phase matching condition. This enhanced spectral component (which occurs in the normal dispersion regime of the fiber) is sometimes also referred to as a "Cherenkov" radiation or soliton-induced resonant emission. Cherenkov radiation is a terminology borrowed from particle physics and it appears when a particle travels faster than the phase velocity of light in the medium. The radiation is emitted at an angle with respect to the trajectory of the particle (whose dimensions are assumed to be much smaller than the wavelength) and the angle is determined by phase matching conditions.

The analogy of this effect in optical waveguides is the resonance that occurs between the pulse, which travels at its group velocity, and the dispersive wave resulting in an energy transfer from the soliton to the dispersive wave at a frequency ω_d dictated by the appropriate phase matching condition [14].

Cherenkov radiation is emitted at the frequency ω_{Ch} at which phase $\phi(\omega_{Ch})$ matches that of the soliton $\phi(\omega_s)$ at the frequency ω_s. Then, the frequency of the Cherenkov radiation is governed by a phase-matching condition requiring that the dispersive waves propagate at the same phase velocity that of soliton. Regarding that the phase of an optical pulse at frequency ω changes as $\phi = k(\omega)z - \omega t$, the two phases at a distance z after a delay $t = z/v_g$ are given by [3]

$$\phi(\omega_{Ch}) = k_{Ch}(\omega_{Ch})z - \omega_{Ch}(z/V_g), \tag{3.21}$$

$$\phi(\omega_s) = k_s(\omega_s)z - \omega_{Ch}(z/V_g) + \frac{1}{2}\gamma P_0 z, \tag{3.22}$$

where V_g is the group velocity of the soliton and $k_{Ch,s}$ is the wave number of the Cherenkov radiation [15]. When the phase matching is achieved, the corresponding soliton emits the Cherenkov radiation and it is possible to estimate the central wavelength and the peak power of the Cherenkov radiation[16] as

$$\lambda_{Ch}(\delta_3) \approx \left[\left(\frac{1 + 4\delta_3^2\,(2N-1)^2}{4\pi\delta_3 T_0}\right) + \nu_s\right]^{-1} c, \tag{3.23}$$

$$P_{Ch}(\delta_3) \approx P_0 \left(\frac{5\pi N}{4\delta_3}\right)^2 \left(1 - \frac{2\pi\,(2N-1)\,\delta_3}{5}\right)^2 exp\left(\frac{-\pi}{2\,(2N-1)\,\delta_3}\right), \tag{3.24}$$

where c is the speed of light, $\nu_s = c/\lambda_s$ is the carrier frequency of the soliton and the coefficient $\delta_3 = \beta_3/(6T_0|\beta_2|)$ is referred as the normalized third order dispersion (TOD). It was demonstrated that Eqs. 3.23 and 3.24 can be used to estimate the frequency and amplitude of Cherenkov radiation under realistic conditions [16], but are valid only for relatively small values of δ_3 due to their perturbative nature. Figure 3.4 shows the corresponding dynamics of such a soliton (with $N \sim 1$) and the emitted Cherenkov radiation in a uniformly SMF.

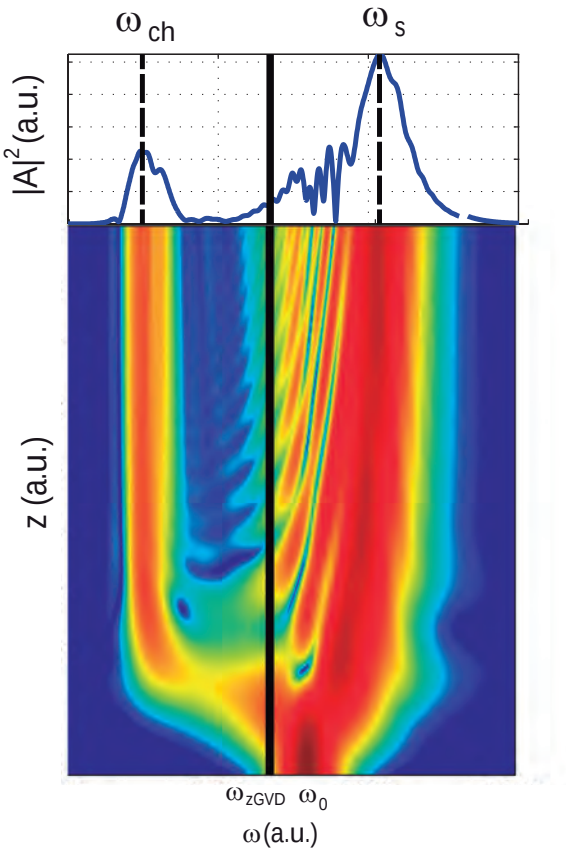

Figure 3.4: (a) Spectral evolution in a uniform SMF. The black line represents the zGVD wavelength.

3.6 Soliton self-frequency shift

Among the above higher-order phenomena acting in SC generation, the soliton self-frequency shift (SSFS) effect becomes one of the most relevant [3]. The SSFS is a self-induced red-shift in the pulse spectrum arising from intrapulse Raman scattering (IRS). The long wavelength components of the pulse experience Raman gain at the expense of the short-wavelength components, resulting in an increasing red-shift as the pulse propagates (see fig. 3.5).

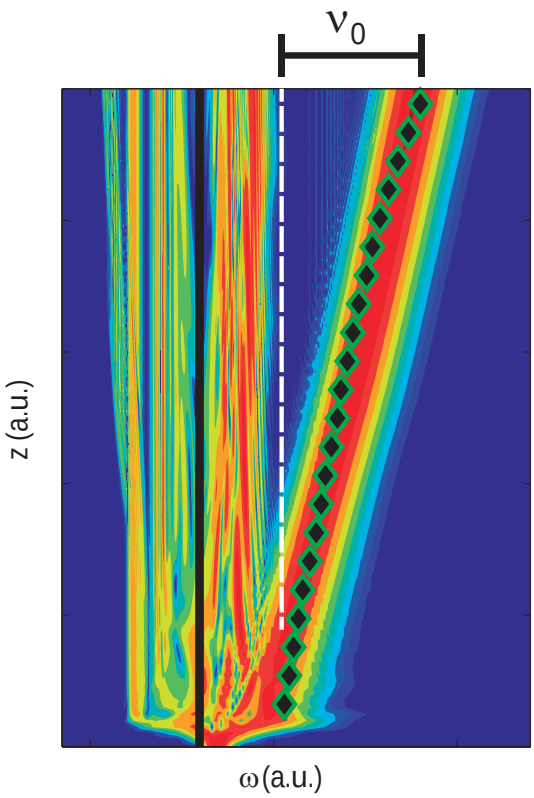

Figure 3.5: Spectral evolution of a soliton in a uniform SMF. Diamonds represents the continuous shift to longer wavelengths from the soliton self-frequency shift based on the Gordon equation 3.25. The black line represents the zGVD wavelength.

After the initial fission, each constituent soliton experiences a continuous shift to longer wavelengths from the soliton self-frequency shift because the individual

soliton bandwidths overlap the Raman gain. As it is shown by Gordon [18], the dynamics of the frequency shift ν_0 can be expressed as

$$\frac{d\nu_0}{dz}\,[THz/km] = -\frac{10^5\lambda^2 D}{16\pi c T_0^3}\int_0^\infty \Omega^3 d\Omega\; \tilde{R}\left(\frac{\Omega}{2\pi T_0}\right) / \sinh^2\left(\frac{\pi\Omega}{2}\right). \qquad (3.25)$$

A consequence of this is that the shorter-duration solitons that are ejected earlier in the fission process experience greater self-frequency downshifts and walkoff proportionally faster from the input pump wavelength.

The pulses eventually separate so that the individual fundamental solitons are seen distinctly at the fiber output. We have found that soliton separation begins to become apparent in the temporal and spectral characteristics after a propagation distance of typically $\sim 5L_D$. However, observing distinct signatures of all N solitons in both time and frequency domains can require significantly further propagation.

References

[1] C. C. Wang, *"Transmission of a Gaussian pulse in single-mode fiber systems,"* J. Lightwave Technol. **1**, 572 - 579 (1983). 26

[2] F. P. Kapron and D. B. Keck, *"Pulse transmission through a dielectric optical waveguide,"* Appl. Opt. **10**, 1519-1523 (1971). 26

[3] G. P. Agrawal, *Nonlinear Fiber Optics, 4th ed.* (Academic Press. 2007). 27, 30, 32, 35, 37

[4] R. H. Stolen and C. Lin, *"Self-phase modulation in silica optical fibers,"* Phys. Rev. A **17**, 1448–1453 (1978). 28

[5] N. Kikuchi and S. Sasaki, *"Analytical evaluation technique of self-phase modulation effect on the performance of cascaded optical amplifier,"* J. Lightwave Tech. **13**, 868–878 (1995). 28, 32

[6] A. R. Chraplyvy, D. Marcuse, and P. S. Henry, *"Carrier induced phase noise in angle-modulated optical fiber systems,"* J. Lightwave Tech. **2**, 6-10 (1984). 29

[7] H. A. Haus, *"Optical fiber solitons: their properties and uses,"* Proc. IEEE, **81**, 970–983 (1993). 31

[8] A. Biswas and S. Konar, *"Soliton-solitons interaction with Kerr law nonlinearity,"* J. Electromagnetic Wave, **19**, 1443–1453 (2005). 31

[9] N. Kikuchi, K. Sekine, and S. Saski, *"Analysis of XPM effect on WDM transmission performance,"* Electron. Lett. **33**, 653–654 (1997). 31

[10] Y. Kodama and A. Hasegawa, *"Nonlinear Pulse Propagation in a Monomode Dielectric Guide,"* IEEE J. Quantum Elect. **23,** 510-524 (1987). 33

[11] E. M. Dianov, Z. S. Nikonova, A. M. Prokhorov, and V. N. Serkin, *"Optimal compression of multi-soliton pulses in optical fibers,"* Sov. Tech. Phys. Lett. **12,** 756–760 (1986). 33

[12] C. M. Chen and P. L. Kelley, *"Nonlinear pulse compression in optical fibers: Scaling laws and numerical analysis,"* J. Opt. Soc. Am. B **19,** 1961–1967 (2002). 33

[13] P. K. A. Wai, C. R. Menyuk, Y. C. Lee, and H. H. Chen, *"Nonlinear pulse propagation in the neighborhood of the zero-dispersion wavelength of monomode optical fibers,"* Opt. Lett. **11,** 464–466 (1986). 34

[14] N. Akhmediev and M. Karlsson, *"Cherenkov radiation emitted by solitons in optical fibers,"* Phys. Rev. A **51,** 2602–2607 (1995). 34, 35

[15] D.V. Skryabin and A.V. Yulin *"Theory of generation of new frequencies by mixing of solitons and dispersive waves in optical fibers,"* Phys. Rev. E **72,** 016619 (2005). 34, 35

[16] S. Roy, S.K. Bhadra and G.P Agrawal, *"Dispersive wave generation in super-continuum process inside nonlinear microstructured fibre,"* Curr. Sci. **100,** 321-342 (2011). 34, 35, 36

[17] P. K. A. Wai, C. R. Menyuk, H. H. Chen, and Y. C. Lee, *"Soliton at the Zero-Group-Dispersion Wavelength of a Single-Model Fiber,"* Opt. Lett. **12,** 628-630 (1987). 34

[18] J. P. Gordon, *"Theory of the soliton self-frequency shift,"* Opt. Lett. **11,** 662–664 (1986). 38

4

Spectra generation by Cherenkov radiation

The growing interest in building light sources for OCT has led to investigation into several methods to achieve multi-peak spectra. In some of these approaches a specific laser source is required for each of the spectral peaks [1, 2], and in others specific filters are applied to white light emission diode (LED) sources [3]. Therefore these methods have an independent control on the frequency of the bands which can be in principle largely detuned to each other, but they are, on the other hand, dependent on many sources and relatively complex setups. The advantage presented by the method we propose in this paper is that only one light (laser) source is needed to produce several localized spectral peaks with distributed power at the same time that they correspond to optical pulses with *bell-shaped* profiles produced with cheap components.

After the soliton fission, when the Raman soliton is shifted to redder region, a radiation (anti-Stokes) that overlaps temporally with this Raman soliton rises and lies in the normal-GVD (spectral components on the short wavelength in this case) regime of the fiber. This radiation is known as the *Cherenkov radiation*, *dispersive waves* (DWs) or as the *nonsolitonic radiation* (NSR). It is emitted at a frequency at which its propagation constant (or phase velocity) matches that of the soliton. The wavelength of the NSR is governed by a simple phase-matching condition requiring that the dispersive waves propagate at the same phase velocity as the soliton.

4. SPECTRA GENERATION BY CHERENKOV RADIATION

To fully exploit the nonlinear dynamics associated to Supercontinuum (SC) generation in optical fibers (see Refs. [4, 5] for reviews on the topic) it is customary to use photonic crystal fibers (PCFs), since they provide a versatile platform to accurately tune the linear and nonlinear effects governing the propagation of optical pulses [6, 7, 8]. However, other simpler and cheaper fiber designs can also yield wide spectra and provide certain control on the pulse propagation dynamics [9, 10], which may suffice for many applications. Nowadays, one of the aspects in SC generation receiving substantial interest is the management of the spectral output to obtain blue and infrared (IR) extended spectra [11, 12, 13, 14], both effects associated to the red-shifting Raman solitons with trapped DWs [15]. Another important attribute to control in less broad spectra is the localization of spectral power in bands centered at specific target wavelengths, consisting on either dispersive waves [16, 17] or Raman solitons in the IR [18]. In the former case, the Cherenkov or dispersive radiation, emitted by solitons under the right phase matching conditions [19], is used as a suitable spectral peak generator. Although multi-peak Cherenkov spectra are automatically generated in both normal and anomalous group velocity dispersion (GVD) regions in the context of SC generation with bright [4, 5] and dark [20] solitons, these methods in general lack of control on the individual carrier wavelengths of the Cherenkov DWs.

In this chapter, we exhibit a method to design a non-uniform fiber to obtain discrete spectral peaks from the DWs emitted by solitonic pulses by an on/off switch of Cherenkov radiation. This cheap method consists in splicing few pieces of standard telecom single mode fiber (SMF) with different cladding diameters, which can be achieved easily via post processing techniques that provide control on the GVD [21, 22]. For the pump, we consider the short pulses provided by a standard Ti:Sapphire laser. Switching on and off the Cherenkov radiation is achieved by adjusting the spectral distance between the zero GVD wavelength, λ_{zGVD}, and the Raman shifting soliton carrier, λ_s, which dramatically controls the radiation efficiency [23]. Several Cherenkov peaks emitted from a single soliton are possible because of the interplay between Raman and recoil induced red-shift, and the λ_{zGVD} management. Such management has proven very useful for manipulating the soliton propagation dynamics, e.g, pulse compression [24], trapping of the Cherenkov radiation in the absence of Raman effect [25], controlling DW

generation in the SC dynamics [26], and generation of a powerful continuum of Cherenkov radiation shed by a single soliton pulse [27]. Practical and low cost methods to tailor the λ_{zGVD} in fibers consist in immersing them in different liquids [28] or reducing their cladding diameter by using chemical etching methods that achieve submicron-diameters [29]. We have used the latter idea, for illustrative purposes, and have computed the linear dispersions and nonlinear coefficients of several SMFs with different cladding diameters (see Fig. 4.1). We envisage that this spectral peak generator will be useful for applications in areas such as optical coherence tomography (OCT) [30, 31], spectroscopy [32], multi-spectral imaging [33, 34, 35], and applications where spectral peaks are required to carry few hundreds of Watts and to present Gaussian-like bell shapes.

4.1 Pulse propagation in non-uniform fiber

We simulate the propagation of fs-pulses with complex amplitude $A(z,T)$ by integrating numerically the Eq. 2.2. This equation accounts for the linear dispersion through the coefficients $\beta_q \equiv d^q\beta(\omega)/d\omega^q|_{\omega=\omega_0}$ (up to $q = 10$) evaluated at the pump frequency $\omega_0 = 2\pi c/\lambda_0$ (where $\lambda_0 = 1060$ nm) of the laser. Nonlinearity is included through the parameter γ and the response function $R(T) \equiv [1 - f_R]\delta(T) + f_R h_R(T)\Pi(T)$, where $f_R = 0.18$, h_R is the commonly used Raman response of silica [36], and $\delta(T)$ and $\Pi(T)$ are the Dirac and Heaviside functions, respectively. The definition of the nonlinear parameter used here constitutes a good approximation for our large-core fibers (see Fig. 4.1), and therefore we do not need to use the recently experimentally [37] and numerically [38] tested coefficients for sub-wavelength waveguides. The input pulses in our modeling are taken as $A(z = 0, T) \equiv \sqrt{P_0}\,\mathrm{sech}(T/T_0)$ with $P_0 \equiv P(z = 0) = 10$ kW and full width at half maximum (FWHM) $\tau_{FWHM} = 65$ fs ($T_0 \equiv \tau(z = 0) \equiv \tau_{FWHM}/2\ln[1+\sqrt{2}] \approx 36.85$ fs). With these parameters, the soliton order, $N \equiv \tau[\gamma P/|\beta_2|]^{1/2}$, is kept below fission threshold, $1 \leq N < 2$, for the input conditions.

Fig. 4.1 shows the nonlinear parameter, $\gamma(\lambda)$, and the lower order dispersion coefficients, $\beta_{2,3}(\lambda)$, for the different segments of our SMF, with different cladding diameters, computed using Optiwave [39]. The key role played by the position

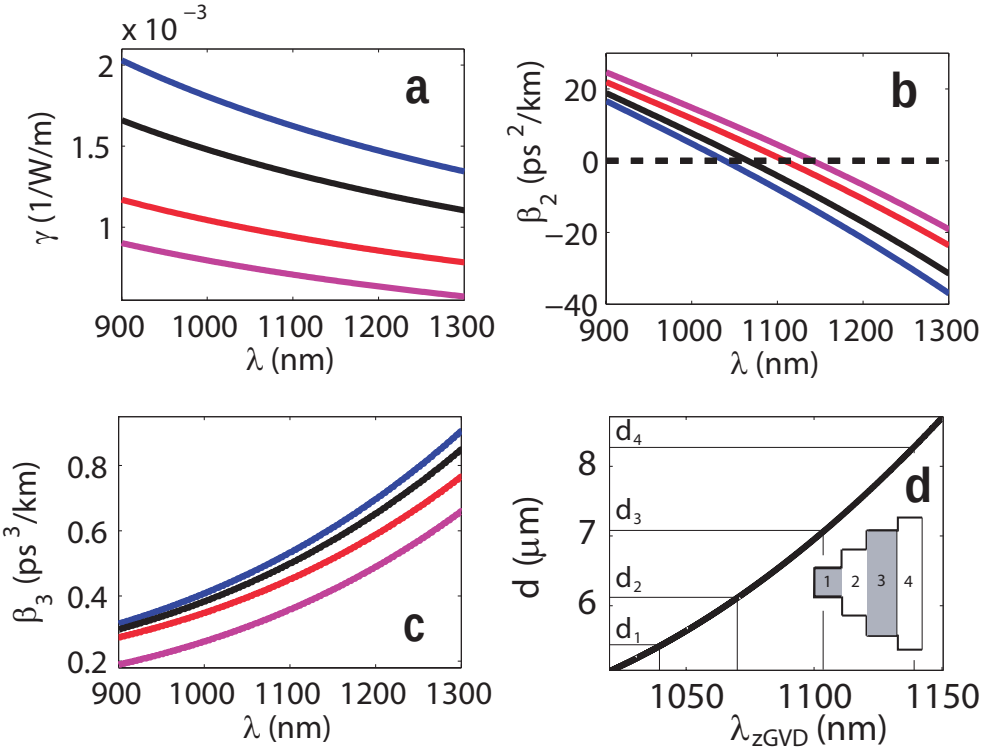

Figure 4.1: (a) Nonlinear coefficient, (b) GVD, and (c) third order dispersion (TOD) for the different cladding diameters: $d = 5.4$ (blue), 6.1 (black), 7.1 (red) and 8.3 μm (magenta). The corresponding values of λ_{zGVD} are: 1035, 1070, 1105, and 1140 nm (see b). (d) Dependence of the cladding diameter, d, on λ_{zGVD}. Inset shows a schematic side view of the non-uniform fiber, in which light propagation occurs from left to right (see Fig. 4.3(a)). Diameters, d, and lengths, L, of the different regions are chosen as: $d_1 = 5.4$, $d_2 = 6.1$, $d_3 = 7.1$, $d_4 = 8.3$ μm; $L_1 = 35$, $L_2 = 40$, $L_3 = 55$, $L_4 = 90$ cm.

of λ_{zGVD} along propagation in the radiation switch on/off requires to have a fine control of it. From our numerical data of dispersion in Fig. 4.1b, it is possible to find a convenient fit to link it with the SMF cladding diameter, d (see Fig. 4.1d):

$$d(\mu m) \cong 8.6434 \times 10^{-5}\lambda_{zGVD}^2(nm) - 1.5958 \times 10^{-1}\lambda_{zGVD}(nm) + 77.9036, \tag{4.1a}$$

$$\lambda_{zGVD}(z) \approx \lambda_s \left[1 + \frac{\lambda_s}{12\pi c\delta_3\tau}\right]^{-1}, \tag{4.1b}$$

where $\delta_3 \equiv \beta_3/6\tau|\beta_2|$ is the z-dependent normalized TOD coefficient.

4.2 Generation of discrete Cherenkov spectra

The matching condition $\beta_{Ch}(\lambda) \equiv \beta_s(\lambda)$ can be expressed approximately for small δ_3 by [40]

$$\lambda_{Ch}(\delta_3) \approx \left[\frac{1 + 4\delta_3^2\,(2N-1)^2}{4\pi\delta_3\tau c} + \frac{1}{\lambda_s}\right]^{-1}, \tag{4.2}$$

and may be visualized by plotting the soliton and radiation dispersion relations, $k_s = \gamma P/2$ and $k_{Ch} = \sum_{q\geq 2}\tilde{\beta}_q(\omega-\omega_s)^q/q!$, versus wavelength [5], as shown in Fig. 4.2a for several stages of the propagation in the non-uniform fiber (see Fig. 4.3).

Fig. 4.3 shows spectral and temporal evolution of a $N(z=0) \approx 1.7$ pulse along the non-uniform SMF consisting of four pieces (see Fig. 4.1d). At the entrance of each of the four pieces the solitons emit blue shifted dispersive radiation during a very short propagation distance, before the recoil effect sharply the solitons red-shifts and the Cherenkov radiation emission is frustrated [5]. In Fig. 4.3(a), after this first fast process, the only role played by the fiber segment with uniform cross section is that of decreasing the soliton frequency through the Raman induced soliton self-frequency shift (SSFS) [41]. This is however, together with the recoil effect, the mechanism we benefit from to tune the soliton wavelength. By tracking $\lambda_s(z)$ and $\tau(z)$ along propagation in a given segment of the SMF, we can efficiently generate a new Cherenkov spectral peak at a desired

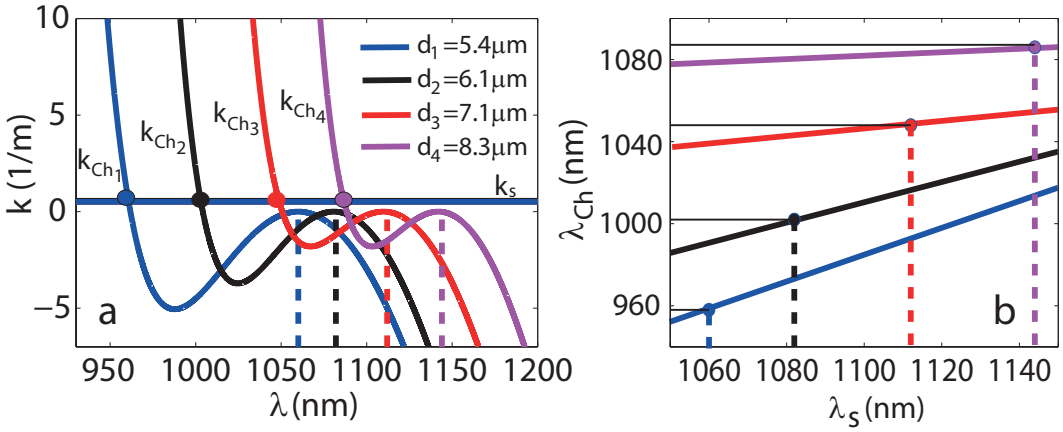

Figure 4.2: (a) Phase matching between the fundamental soliton k_s (straight line) and the DWs k_{Ch} for different diameters (curves), and (b) dependence of λ_{Ch} on λ_s in the decreasing cladding diameter SMF with $d_1 = 5.4$ (blue), $d_2 = 6.1$ (black), $d_3 = 7.1$ (red), and $d_4 = 8.3$ μm (magenta). Dots indicate the corresponding Cherenkov radiation wavelength, λ_{Ch}, and dashed lines mark the soliton central wavelength, λ_s. The four cases considered here correspond to the distances at which the soliton enters a new SMF segment (see Fig. 4.3a).

wavelength, λ_{zGVD} (red-shifted from the previous one, see Fig. 4.2), by splicing a new SMF segment with d given by combining the reflected δ_3 of Eq. 4.2,

$$\delta_3 \approx \frac{\pi c\tau \left[\frac{1}{\lambda_{Ch}} - \frac{1}{\lambda_s}\right] + \sqrt{\pi^2 c^2 \tau^2 \left[\frac{1}{\lambda_{Ch}} - \frac{1}{\lambda_s}\right]^2 - [2N-1]^2}}{2\,[2N-1]^2}, \tag{4.3}$$

together with Eqs. 4.1a-4.1b. In obtaining Eq. 4.3 we restricted ourselves to the case $\delta_3 > 0$ (i.e., around the first zero GVD wavelength). Note that in our problem, the analytical method of Ref. [41] can not be used to predict accurately the carrier frequency of the soliton after certain propagation distance because the radiation emission induces spectral recoil and a drift in the soliton order, N (see Fig. 4.3c).

Despite the low initial value for the soliton order, $1 \leq N(z=0) < 2$, and the fact that it releases energy in the form of Cherenkov waves, the frequency conversion keeps being highly efficient due to the decrease in $|\beta_2(\lambda_s)|$ at the entrance of each of the new fiber segment, which keeps $N > 1$ (see Fig. 4.3c).

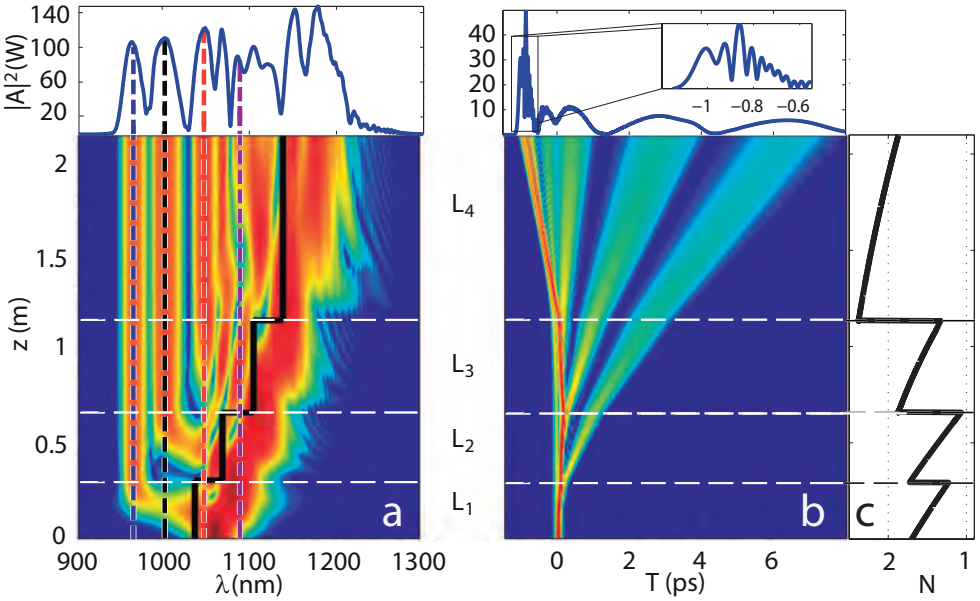

Figure 4.3: (a) Spectral and (b) temporal evolution of an input pulse at $\lambda_0 = 1060$ nm with $P_0 = 10$ kW and a width of 65 fs (FWHM). The shifting λ_{zGVD} (initially at 1035 nm) is marked by the solid black line in (a) and the vertical dashed correspond to the λ_{Ch} predicted by eq. 4.2: 958 (blue), 1002 (black), 1048 (red) and 1086 nm (magenta). (c) Evolution of the soliton order, N, for each fiber segment of length L_j. The value of $1 \leq N < 2$ is approximately the same for both solitons resulting from fission by the end of the last segment, L_4 (both $N(z)$ lines overlap). Spectral and temporal outputs are shown on top.

This defines the limiting factor of the device: N is kept > 1 because $|\beta_2(\lambda_s)|$ is decreased by moving the λ_{zGVD} closer to λ_s, however this is valid as long as λ_{zGVD} does not fall within the soliton spectral width (e.g., within its spectral FWHM). At the beginning of the fourth segment, the drastic change of the λ_{zGVD} causes an increase of $N \sim 2.3$ and the subsequent fission into two fundamental solitons (see Fig 4.3a).

Because the short pulses we consider here ($T_0 < 50$ fs), the Raman gain induces an additional perturbation to solitons and they release strong radiation in the form of Airy waves [42], which carrier frequency is in the anomalous GVD and slightly above than that of the soliton. In our non-uniform fiber the solitons can trap these waves[43], which may be used as additional spectral peaks since

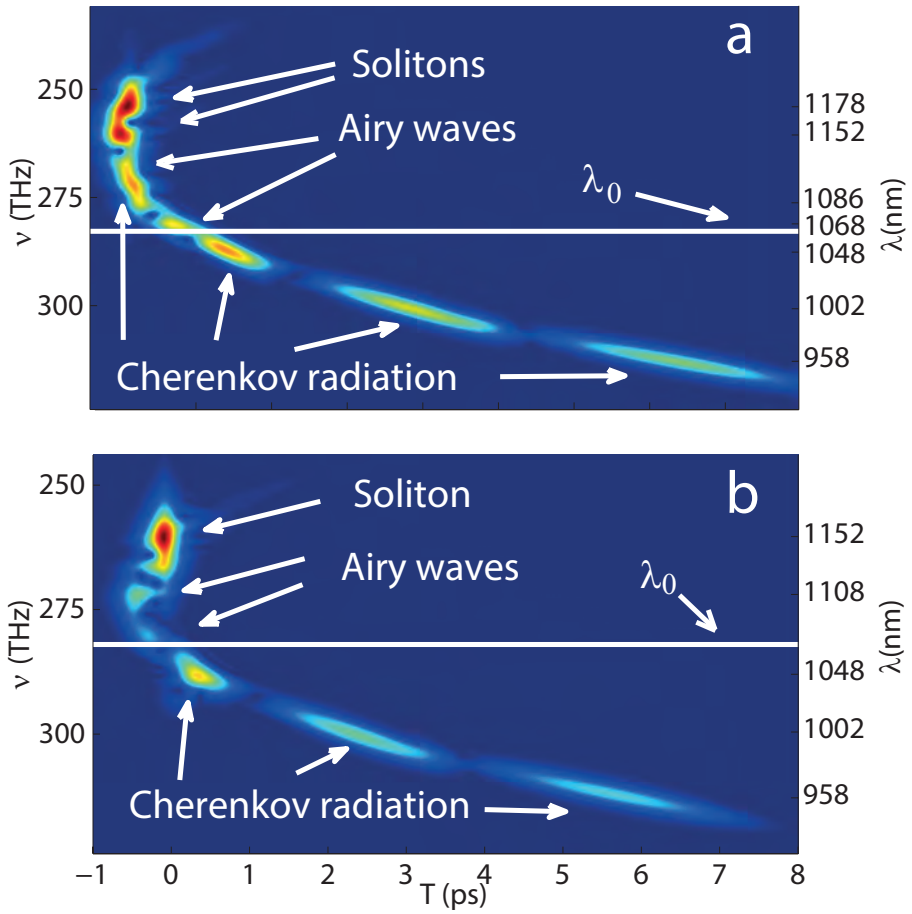

Figure 4.4: XFROG traces for the output field at $z = 2.1$ m of (a) Fig. 4.3a and (b) Fig. 4.3b. Horizontal white lines mark the pump.

being trapped they maintain a localized shape in the time domain. To show that the peaks generated here are localized in both time and frequency, we plot in Fig. 4.4a the XFROG corresponding to the final stage of the propagation at $z = 2.1$m. Spectrogram is computed as $\sum(\omega, T) = |\int_{-\infty}^{\infty} A(T')g(T' - T)e^{-i\omega T'}dT'|$, where the gate function is $g(\zeta) = \mathrm{sech}(\zeta/\tau_g)$ with $\tau_g = 30$ fs. If the tunneling of Airy waves through the soliton is not desired, it is possible to avoid it by elongating the third section of the fiber, thus keeping them separated in time domain from the Cherenkov radiation by the soliton. This is shown in the Fig. 4.4b. Simultaneous temporal and spectral representation of light states can be experimentally measured with great resolution and quality [44], providing evidence of the right

performance of the non-uniform fiber spectral peak generator.

References

[1] J.N. Farmer and C.I. Miyake, *"Method and apparatus for optical coherence tomography with a multispectral laser source,"* U.S. Patent 6,538,817 filed October 17, 2000, and issued March 25, 2003. 41

[2] J.M. Huntley, P.D, Ruiz, and T. Widjanarko, *"Apparatus for the absolute measurement of two dimensional optical path distributions using interferometry,"* U.S. Patent 2,011,010,092 filed July 20, 2010, and issued July 12, 2012. 41

[3] N.L. Everdell, I.B. Styles, A. Calcagni, J. Gibson, J. Hebden, and E. Claridge, *"Multispectral imaging of the ocular fundus using light emitting diode illumination,"* Rev. Sci. Instrum. **81,** 093706-093706-9 (2013). 41

[4] J. M. Dudley, G. Genty, and S. Coen, *"Supercontinuum generation in photonic cristal fibers,"* Rev. Mod. Phys. **78,** 1135–1184 (2006). 42

[5] V. Skryabin, and A.V. Gorbach, *"Colloquium Looking at a soliton through the prism of optical supercontinuum,"* Rev. Mod. Phys. **82,** 1287–1299 (2010). 42, 45

[6] P. Russell, *"Photonic crystal fibers,"* Science **17,** 358-362 (2003). 42

[7] W. H. Reeves, D. V. Skryabin, F. Biancalana, J. C. Knight, P. St. J. Russell, F. G. Omenetto, A. Efimov, and A. J. Taylor, *"Transformation and control of ultra-short pulses in dispersion-engineered photonic crystal fibres,"* Nature **424,** 511-515 (2003). 42

[8] J. C. Knight, *"Photonic crystal fibres,"* Nature **424,** 847-851 (2003). 42

[9] T. A. Birks, W. J. Wadsworth, and P. St. J. Russell, *"Supercontinuum generation in tapered fibers,"* Opt. Lett. **25,** 1415–1417 (2000). 42

[10] W. J. Wadsworth, A. Ortigosa-Blanch, J. C. Knight, T. A. Birks, T.-P. Martin Man, and P. St. J. Russell, *"Supercontinuum generation in photonic crystal fibers and optical fiber tapers: a novel light source,"* J. Opt. Soc. Am. B **19,** 2148-2155 (2002). 42

[11] A. C. Judge, O. Bang, B. J. Eggleton, B. T. Kuhlmey, E. C. Mägi, R. Pant, and C. Martijn de Sterke, *''Optimization of the soliton self-frequency shift in a tapered photonic crystal fiber,"* J. Opt. Soc. Am. B **26,** 2064-2071 (2009). 42

[12] A. Kudlinski, M. Lelek, B. Barviau, L. Audry, and A. Mussot, *"Efficient blue conversion from a 1064 nm microchip laser in long photonic crystal fiber tapers for fluorescence microscopy,"* Opt. Express **18,** 16640-16645 (2010). 42

[13] C. Cheng, Y. Wang, Y. Ou, and Q. lv, *"Enhanced red-shifted radiation by pulse trapping in photonic crystal fibers with two zero-dispersion wavelengths,"* Opt. Laser. Technol. **44,** 954-959 (2012). 42

[14] S. T. Sörensen, U. Müller, C. Larsen, P. M. Moselund, C. Jakobsen, J. Johansen, T. V. Andersen, C. L. Thomsen, and O. Bang, *"Deep-blue supercontinuum sources with optimum taper profiles: A verification of GAM,"* Opt. Express **20,** 10635-10645 (2012). 42

[15] A. V. Gorbach and D. V. Skryabin, *"Light trapping in gravity-like potentials and expansion of supercontinuum spectra in photonic-crystal fibres,"* Nat. Photon. **1,** 1749-4885 (2007). 42

[16] G. Moltó, M. Arevalillo-Herráez, C. Milián, M. Zacarés, V. Hernández, and A. Ferrando, *"Optimization of supercontinuum spectrum using genetic algorithms on service-oriented grids,"* in *Iberian Grid Infrastructures Conference proceedings* ISBN 978-84-9745-406-3, pp. 137–147 (2009). 42

[17] A. Ferrando, C. Milián, N. González, G. Moltó, P. Loza, M. Arevalillo-Herráez, M. Zacarés, I. Torres-Gómez, and V. Hernández, *"Designing supercontinuum spectra using Grid technology,"* Proc. SPIE **7839,** 78390W (2010). 42

[18] S. A. Dekker, A. C. Judge, R. Pant, I. Gris-Sánchez, J. C. Knight, C. Martjn de Sterke, and B. J. Eggleton, *"Highly-efficient, octave spanning soliton self-frequency shift using a specialized photonic crystal fiber with low OH loss,"* Opt. Express **19,** 17766-17773 (2011). 42

[19] N. Akhmediev and M, Karlsson, *"Cherenkov radiation emitted by solitons in optical fibers,"* Phys. Rev. A **51,** 2602-2607 (1995). 42

[20] C. Milián, D. V. Skryabin, and A. Ferrando, *"Continuum generation by dark solitons,"* Opt. Lett. **34,** 2096-2098 (2009). 42

[21] R. Zhang, X. Zhang, D. Meiser, and H. Giessen, *"Mode and group velocity dispersion evolution in the tapered region of a single-mode tapered fiber,"* Opt. Express **12,** 5840-5849 (2004). 42

[22] C. M. B. Cordeiro, W. J. Wadsworth, T. A. Birks, and P. St. J. Russell, *"Engineering the dispersion of tapered fibers for supercontinuum generation with a 1064 nm pump laser,"* Opt. Lett. **30,** 1980–1982 (2005). 42

[23] F. Biancalana, D. V. Skryabin, and A. V. Yulin , *"Theory of the soliton self-frequency shift compensation by the resonant radiationin photonic crystal fibers,"* Phys. Rev. E **70,** 016615 (2004). 42

[24] J. C. Travers, J. M. Stone, A. B. Rulkov, B. A. Cumberland, A. K. George, S. V. Popov, J. C. Knight, and J. R. Taylor, *"Optical pulse compression in dispersion decreasing photonic crystal fiber,"* Opt.Express **15,** 13203-13211 (2007). 42

[25] J.C. Travers and J.R. Taylor, *"Soliton trapping of dispersive waves in tapered optical fibers,"* Opt. Lett. **34,** 115-117 (2009). 42

[26] S. Pricking and H. Giessen, *"Tailoring the soliton and supercontinuum dynamics by engineering the profile of tapered fibers,"* Opt. Express **18,** 20151-20163 (2010). 43

[27] C. Milián, A. Ferrando, and D. V. Skryabin, *"Polychromatic Cherenkov radiation and supercontinuum in tapered optical fibers,"* J. Opt. Soc. Am. B **29,** 589–593 (2012). 43

[28] R. Zhang, J. Teipel, X. Zhang, D. Nau, and H. Giessen, *"Group velocity dispersion of tapered fibers immersed in different liquids,"* Opt. Express **12,** 1700-1707 (2004). 43

[29] H.J. Kbashi, *"Fabrication of Submicron-Diameter and Taper Fibers Using Chemical Etching,"* J. Mater. Sci. Technol. **28,** 308 - 312 (2012). 43

[30] J.G. Fujimoto, C. Pitris, S. A. Boppart, and M.E, Brezinski, *"Optical coherence tomography: An emerging technology for biomedical imaging and optical biopsy,"* Neoplasia **2,** 9-25 (2000). 43

[31] P. Cimalla, J. Walther, M. Mehner, M. Cuevas, and E. Koch, *"Simultaneous dual-band optical coherence tomography in the spectral domain for high resolution in vivo imaging,"* Opt. Express **17,** 19486-19500 (2009). 43

[32] E. Lareau, F. Lesage, P. Pouliot, D. Nguyen, J. Le Lan, and M. Sawan, *"Multichannel wearable system dedicated for simultaneous electroencephalography/near-infrared spectroscopy real-time data acquisitions,"* J. Biomed. Opt. **16,** 096014-096014-14 (2011). 43

[33] A.M Smith, M.C. Mancini, and S. Nie, *"Bioimaging: Second window for in vivo imaging,"* Nat. Nanotechnol. **9,** 1748-3387 (2009). 43

[34] J.M. Huntley, T. Widjanarko, and P.D. Ruiz, *"Hyperspectral interferometry for single-shot absolute measurement of two-dimensional optical path distributions,"* Meas. Sci. Technol. **21,** 075304 (2010). 43

[35] Q. Cao, N.G. Zhegalova, S.T. Wang, W.J. Akers, and M.Y. Berezin, *"Multispectral imaging in the extended near-infrared window based on endogenous chromophores,"* J. Biomed. Opt. **18,** 101318-101318 (2013). 43

[36] G. P. Agrawal, *Nonlinear Fiber Optics, 4th ed.* (Academic Press. 2007). 43

[37] S. Afshar V., W. Q. Zhang, H. Ebendorff-Heidepriem, and T. M. Monro,, *"Small core optical waveguides are more nonlinear than expected: experimental confirmation,"* Opt. Lett. **34,** 3577-3579 (2009). 43

[38] C. Milián and D. V. Skryabin, *"Nonlinear switching in arrays of semiconductor on metal photonic wires,"* Appl. Phys. Lett. **98,** 111104 (2011). 43

[39] www.optiwave.com. 43

[40] S. Roy, S.K. Bhadra, and G.P Agrawal, *"Dispersive wave generation in supercontinuum process inside nonlinear microstructured fibre,"* Curr. Sci. **100,** 321-342 (2011). 45

[41] J. P. Gordon, *"Theory of the soliton self-frequency shift,"* Opt. Lett. **11,** 662-664 (1986). 45, 46

[42] A.V. Gorbach and D.V. Skryabin, *"Soliton self-frequency shift, non-solitonic radiation and self-induced transparency in air-core fibers,"* Opt.Express **16,** 4858-4865 (2008). 47

[43] A.V. Gorbach and D.V. Skryabin, *"Theory of radiation trapping by the accelerating solitons in optical fibers,"* Phys. Rev. A **76,** 053803 (2007). 47

[44] B. Metzger, A. Steinmann, F. Hoos, S. Pricking, and H. Giessen, *"Compact laser source for high-power white-light and widely tunable sub 65 fs laser pulses,"* Opt. Lett. **35,** 3961-3963 (2010). 48

5

Optimization of Raman frequency conversion and dual-soliton based light sources

The soliton self-frequency shift (SSFS) [1, 2] plays a central role in many effects taking place during supercontinuum (SC) generation in optical fibers (see Refs. [3, 4] for a review on the topic). To mention only a few examples, light trapping [5], multi-peak soliton states [6, 7, 8], emission of Airy waves [9], intense dark-soliton SC [10] or broad and intense blue shifted polychromatic dispersive waves [11], would not be possible (or strong enough) without the SSFS. One of the most notorious features of the Raman effect in SC generation with femtosecond pulses corresponds to the Raman soliton carrying the lowest frequency. Its large frequency shift from the laser pulse has motivated IR-Raman soliton sources [12, 13, 14] and their optimization [15, 16, 17].

In the previous section, we have showed that a fs-pulse pumped in simple single mode fiber (SMF) can generates several pre-defined spectral peaks by means of dispersive waves for potential applications of optical coherence tomography (OCT) around of 1000 nm, typical range for the normal region accesible with the SMF. Now, regarding the same kind of applications, we present a new way of optimization to obtain spectral peaks fixed in selected channels based on the first ejected Raman-soliton with the use of a genetic algorithm (GA).

5. OPTIMIZATION OF RAMAN FREQUENCY CONVERSION AND DUAL-SOLITON BASED LIGHT SOURCES

In this chapter we present an efficient and general computational optimization method based on a GA to find the maximum Raman soliton conversion in a uniform photonic crystal fiber (PCF) NL-2.4-800 (see Fig. 5.1) exhibiting SC generation at the Ti:Sapphire laser wavelengths. The Ti:Sapphire laser is mainly used in scientific research because of their tunability and their ability to generate ultrashort pulses [18]. This method finds the optimal input pulse parameters, namely central wavelength, λ_0, temporal width, T_0, and peak power, P_0, that maximize the output SC power in spectral channels of a fixed width and central frequencies sited in the second near-infrared window (NIR II) also called extended near infrared (exNIR) region which corresponds at 1000 to 1400 nm. Our typical channel width, 50 nm, was chosen narrow enough such that the optimal central channel wavelength (λ_c) will be around the carrier frequency of the most powerful soliton, i.e. the firstly ejected Raman soliton in the IR region. Like previous works [19, 20], the tunability of λ_c represents an important feature of this strategy, since the greatest potential of the given PCF is discovered, which represents a valuable potential for practical applications, specially in situations where limited choice of PCF designs is available.

The inverse problem, i.e. the design of PCFs via GAs to optimize the SC has indeed been previously solved satisfactorily in a wide range of situations [21, 22, 23, 24, 25]. Our interest in the IR region is motivated by the applications in OCT [26, 27, 28, 29, 30, 31, 32], specially imaging in the NIR II [33, 34]. Given the large amount of simulations required by this method, distributed computing (a Grid platform) was used to reduce the time required to find the optimal solutions. The advantage of this infrastructure is that it allows the use of the same code in a platform of scalable resources (number of processors, etc.), which are adapted according to the needs of the particular optimization problem. We obtain several peaks joining the first ejected Raman soliton because of the non-trivial behavior of the SC in the anomalous region and the high-order soliton originated. Additional peaks can be used as a plus in the tuneable optical source.

5.1 Supercontinuum modeling and genetic algorithm

We simulate the nonlinear propagation of the complex electric field envelope, A, along the fiber axis, z, by integrating numerically (with Runge-Kutta method) the Eq. 2.2, where the β_q's account for the linear fiber q-order dispersion and

$$\gamma = \frac{\epsilon\epsilon_0^2\omega_0 c}{3}\frac{\int\int dxdy n_2(x,y)[|2\vec{E}|^4 + |\vec{E}^2|^2]}{[\int\int dxdy\,\mathrm{Re}\{\vec{E}\times\vec{H}^*\}\hat{u}_z]^2}, \tag{5.1}$$

is the nonlinear parameter [35] which has been computed with a finite elemente method (FEM) solver by integrating the electromagnetic components of the modal field at $\lambda = 800$ nm along the transverse fiber cross section and using $\epsilon = 2.09$ and $n_2 = 2.6 \times 10^{-20}$ m^2/W for the relative permittivity and nonlinear index of silica glass, respectively. The nonlinear Raman response of the glass is $R(t) = [1 - f_R]\Delta(t) + f_R h_R(t)$ [36], where the Raman (delayed) contribution is weighted by $f_R = 0.18$ and described by

$$h_R(t) = \frac{\tau_1^2 + \tau_2^2}{\tau_1\tau_2^2}\Theta(t)\exp(-\frac{t}{\tau_2})\sin(\frac{t}{\tau_1}), \tag{5.2}$$

where $\tau_1 = 12.2$ fs, $\tau_2 = 32$ fs, and $\Theta(t)$ is the Heaviside step function. The input pulses used in our simulations are of the form $\sqrt{P_0}\,\mathrm{sech}(t/T_0)$.

For each simulation along the PCF, the GA generates an *individual* with the *genome* $\mid g\rangle \equiv [g_1, g_2, g_3]^T = [T_0, \lambda_0, P_0]^T$ (see section 2.2) and evaluates how suitable that individual is from the simulation output through the *fitness* function defined as

$$\phi(\omega_c;\delta) \equiv \left[\int_{\omega_c-\delta}^{\omega_c+\delta} d\omega' |\tilde{A}(\omega')|^2\right]^{-1}, \tag{5.3}$$

where $|\tilde{A}(\omega')|^2$ is the output pulse intensity, $2\delta = 50$ nm is the chosen spectral channel width, that ω_c is the central frequency determined by inspection of the output spectrum to minimizes $\phi(\omega_c;\delta)$.

After an initial set of population threshold p_{th} randomly (uniformly distributed) generated individuals (stage 1), the genetic operators (GO), mutation $\hat{\mathcal{M}}$ and crossover $\hat{\mathcal{X}}$ are responsible of generating the new *offspring* to increase

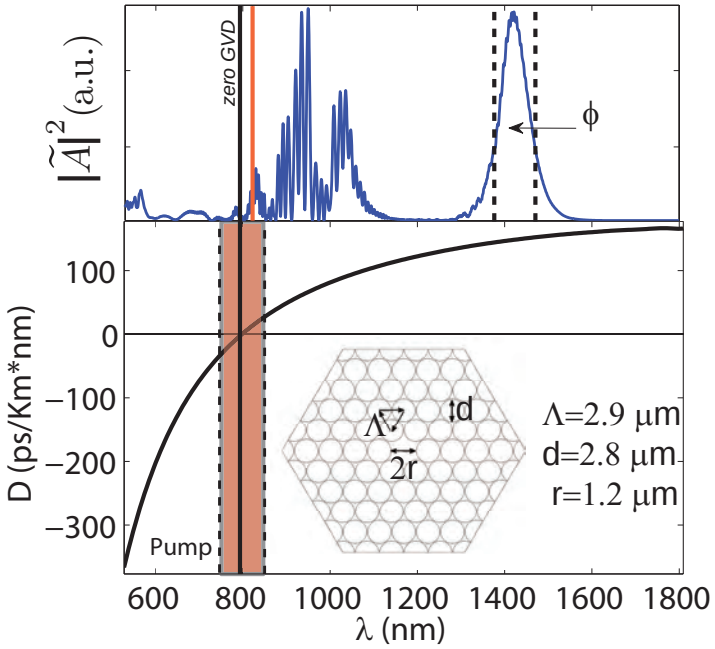

Figure 5.1: Dispersion and cross section of the PCF used in our modeling with the shaded region marking the tunability range of the central wavelength of the pulse. Top figure shows a sample output spectrum with the corresponding channel (delimited by the dashed lines) over which ϕ is evaluated, according to Eq. 5.3. Vertical solid black line marks the *zero GVD* and the red one in the top shows the particular λ_0 of this sample output.

the population size up to $p = p_{max} > p_{th}$ (stage 2), to further make it evolve towards optimal solutions (stage 3). During stages $2 - 3$, to fully exploit the processing power of the Grid, we used a steady state GA, which keeps the Grid constantly computing new individuals in parallel, which are added to the population if $p < p_{max}$ or replace the worst one of the population if $p = p_{max}$ and $\phi_{new} < \phi_{worst}$. We briefly describe the mutation and cross-over operators below (see section 2.2).

5.2 Raman frequency conversion

As mentioned before, the spectral channels in this work are based on OCT applications focused on the NIR II region. It has been proved that high axial resolution

in OCT systems is aimed in the spectral region of 800 nm to 1400 nm [37, 38]. Aditionally, the NIR II light decrease in scattering and increase in transparency of the biological tissues over the NIR range [39]. Moreover Gaussian spectral shapes avoid spurious structures in OCT images [40]. For these reasons, IR-Raman soliton with its characteristic Gaussian shape is founded to be the best option to OCT applications.

We planted the search of external parameters (see section 2.2), λ_0, T_0 and P_0, in section 5.2.1 with the use of our GA (see section 5.1). In order to prove the convenience of our method, it is made an exhaustive search of the best fitness value by scanning the entire ranges of parameters. It is shown in section 5.2.2.

5.2.1 Optimal solution using genetic algorithms

The optimization consisted in the search of parameters that originate the maximum output power in each selected spectral channel on the NIR II using the GA to vary values of the parameters within a given ranges, P varies in the range $[1, 15]$ kW, whereas λ is changed within the interval $[750, 850]$ nm and T in the range of $[30, 110]$ fs. The range of values used in this work are attainable in realistic Ti:Sapphire lasers. The set of all the individuals generated by the GA in each channel optimization is shown as an example in Fig. 5.2(a) in a $3D$ graphic in the space of external parameters with its domain corresponding to the ranges selected.

This *"cloud"* of individuals corresponds to all solutions generated by the GA, their *fitness* function being represented by the color code bar. Lighter points have smaller fitness values (thus, better) than darker ones. We observe that there exists a zone where the GA tends to accumulate points. It is precisely in this region where the best fitness value (red point) is found. It is worth mentioning that some of these regions could contain more candidates to optimal solutions than those eventually selected by the GA. Thus, keeping track of these "quasi-optimal" individuals can also be of great interest from the physical point of view since they can provide extra-local minima of the *fitness* function not considered in a preliminary physical analysis of the optimization scenario. Once the local minima have been detected, a more accurate search around them combining GA

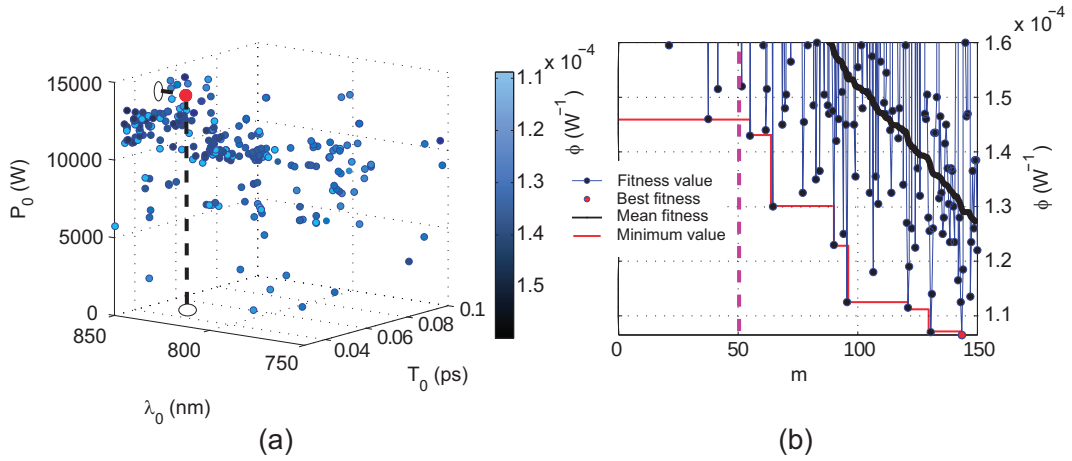

Figure 5.2: (a) Cloud of $m = 150$ individuals generated by the GA for a channel of $\lambda_c = 1225$ nm. The color of the points sketch the fitness value of each individual, lighter points have smaller (thus, better fitness values) and the optimal individual is represented as the red point sited in the coordinates of the three optimized parameters. (b) Typical fitness value (ϕ) evolution of executions in chronological order of generation during the optimization procedure with its mean fitness value (black line) and the minimum global value (red line), dashed magenta vertical line separate the best individual within the first random individuals ($m = p_{th} = 50$) generated in the stage 1 of the process.

strategies and other optimization techniques can be performed in order to find a better minimum of the *fitness* function.

Figure 5.2(b) shows clearly the "dynamical" improvement in the fitness value as the GA evolves. The initial "optimized" value is obtained in the stage 1, when the initial population of 50 individuals is randomly generated (delimited by the vertical dashed line). After the 50th evaluation, the stage 2 of our algorithm initiate, when genetic operators start to act on the previous population. A significant improvement in the fitness of the population is apparent The mean fitness value of the population is monotonically decreasing as new individuals are generated, as the black continuous curve shows. The red line shows the minimum global value until the instant of the last individual is generated in the process. Our GA has not a tendency to converge towards local optima or arbitrary points rather than the global optimum of the problem. This is caused because the operator

of mutation gives a lower probability of occurrence than crossover operator [see Eqs. 2.14 and 2.16]. This combination gives a good diversity in the generation of new individuals with better probability to conserve the best properties of its predecessors ensuring the good convergence of the GA. The best individual for each channel within the final population is taken as the optimized value. The set of optimized parameters for each λ_c within the NIR II region and under the mentioned conditions are shown in Table 5.1.

Table 5.1: Optimal parameters, T_0, λ_0, P_0, obtained using the GA. The soliton order, N, fitness value, ϕ, output central wavelength, λ_c, and efficiency of frequency conversion, η, are shown as the obtained results.

Optimal parameters			Results			
T_0 (fs)	λ_0 (nm)	P_0 (kW)	N	ϕ $(10^{-4}/W)$	λ_c (nm)	$\eta(\%)$
37.09	813.23	7.00	9.06	1.182	1025	21.34
34.54	837.13	6.79	4.94	0.916	1075	24.78
56.18	827.63	8.92	10.70	1.136	1125	24.15
85.09	845.25	7.83	11.83	1.093	1175	21.67
50.45	829.05	14.54	11.96	0.832	1225	26.67
57.97	849.25	13.00	9.94	0.086	1275	21.35
91.51	842.28	14.91	18.17	1.125	1325	24.34
110.00	845.65	14.57	20.87	0.992	1375	24.65

The spectral (λ) and temporal ($T = \frac{t}{t_0}$) evolutions of one resulting optimized external parameters are shown in Figs. 5.3(a)-(b), respectively. The black continuous and dashed lines represent the *zero GVD* and λ_0, respectively, the white dashed lines delimit the spectral channel where the maximum spectral power was found. As expected, the center position of the channel is in accord with the final position of the mean frequency of the first soliton ejected after the soliton fission ($z > L_D/N$).

The maximum spectral power founded for each channel results very approximate to the Kodama and Hasegawa predictions for the soliton amplitude [41]. The multichannel behavior strongly affects the total power captured by the most

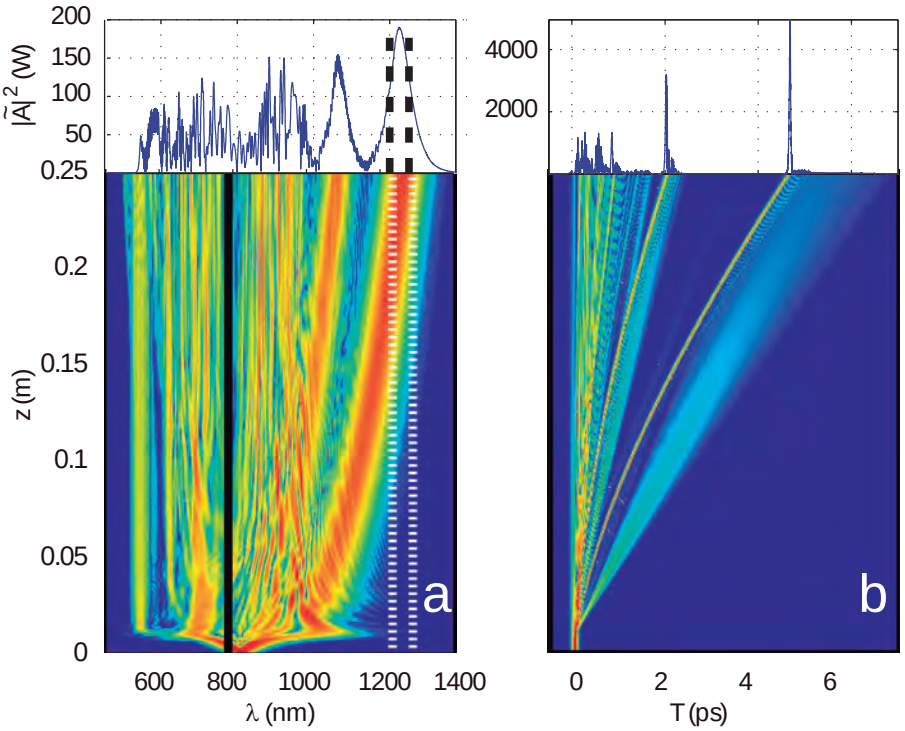

Figure 5.3: Spectral (a) and temporal (b) window evolution on distance z corresponding to optimized parameters $T_0 = 50.45$ fs, $\lambda_0 = 829.05$ nm and $P_0 = 14.54$ kW for a channel centred in $\lambda_c = 1225$ nm (as in Table 5.1). In the spectral window, white dashed vertical lines shows the channel spectrum with maximum spectral power obtained by the GA and the continuous black vertical line indicates the *zero GVD* wavelength.

red-shifted and powerful branch (corresponding to the first initially fissioned soliton), which is increased with respect to that obtained in the initial optimization. It is known that SSFS can be made large by propagating shorter pulses with high peak powers inside highly nonlinear fibers and that the fission of higher-order solitons generates frequency-shifted pulses in form of Raman solitons [1]. This effect can be partly explained by means of Eq.(2.8): T_0 is directly proportional to the soliton order, therefore if T_0 decrease, N will be decreased too. In this context, a physical interpretation of our optimization results shows us that best conversion rates are always achieved when minimal fission (ideally, no fission) of Raman solitons occurs (see Tables 5.2 and 5.3).

This is a physically meaningful result, since keeping SC generation restricted to minimal soliton-generation scenario guarantees the existence of maximum spectral power centred in the desired channel originated from the spectral evolution of the initial pulse (see Figs.5.3 and 5.4). In this way, spectral evolution tends to present a low number of fissioned fundamental solitons at the second part of optimization. The spectral power is thus efficiently concentrated in the channel where less fissioned solitons are shifted by Raman effect.

In order to check the stability of these values we perform a second robust method of optimization. It is shown in the next section.

5.2.2 Optimal solution using exhaustive search

Now, a second method is implemented to check the suitability of the use of GAs described above. It consists in a search of the best fitness of all possible individuals resulting of a systematic evaluation of all possible combinations of parameters existing within the defined ranges and steps ($m = 675$). It is worth mentioning that this process requires larger capabilities in terms of time-machine, even with the use of a GRID platform, it takes $\sim$ 95 h for each channel optimization [see section 5.1]. The set of optimized parameters resulting by the robust method are shown in Table 5.2.

We can see from Tables 5.1 and 5.2 that the efficiency obtained in the optimization using a GA is better than the optimization made without it, even using less number of evaluations, m. As we can see in Fig. 5.2(a), it is visualized the existence of an accumulation points near of the final solution, this feature permits to establish an strategy to reduce the complexity of the problem by focusing only on these smaller regions of interest using the same robust method. Therefore, we perform a new optimization step by selecting a "zoom-in" region around the previously optimized results presented in section 5.2.1. For the search of optimal parameters, we redefine the range of the input parameters in order to scan a smaller neighborhood of the best individual in the *cloud* of solutions. The new conditions are: $P \in [P_0 \pm 0.5]$ kW, $T \in [T_0 \pm 5]$ fs and $\lambda \in [\lambda_0 \pm 5]$ nm. This "zoom-in" was made for each channel and permit to increase the range resolutions, therefore to improve the fitness value and to get a better efficiency conversion in

Table 5.2: Optimal parameters, T_0, λ_0, P_0, obtained for spectral tuning in the initial stage of optimization by exhaustive search with $m = 675$. The soliton order, N, fitness value, ϕ, output central wavelength, λ_c, and efficiency of frequency conversion, η, are shown as the obtained results.

Optimal parameters			Results			
T_0 (fs)	λ_0 (nm)	P_0 (kW)	N	ϕ $(10^{-4}/W)$	λ_c (nm)	$\eta(\%)$
90	810	10	53.32	1.466	1025	17.29
100	810	10	59.24	1.496	1075	15.22
100	850	7	22.03	1.552	1125	17.67
90	830	10	30.69	1.458	1175	16.29
100	850	9	24.98	1.332	1225	16.76
100	850	12	28.84	1.247	1275	14.89
100	850	14	31.15	1.927	1325	14.17
110	850	15	32.32	1.582	1375	15.54

the spectrum output profile. The results of the "zoom-in" optimization process are shown in Table 5.3.

Figure 5.4 shows the espectral and temporal evolution of the "zoom-in" optimization.

Table 5.3 indicates that the efficiency is improved after "zooming-in" of optimal solutions obtained using the entire range but it is not still improved compared to Table 5.1 proving the efficiency of our method.

The chart of values for the $\lambda_c = 1225$ nm case is shown in the fig. 5.5(a).

The black polygonal-line shows how the best individuals jump in random way for each change of parameter value in the case when the use of a GA is avoided. Figure 5.5(b) shows the fitness value evolution in chronological order for the swept process. A *sawtooth* behavior of the fitness value evolution is due to the fitness value becomes better and worse by repeating the parameters values for the individuals while they are evaluated in the swept. The final parameters for this robust test was close to our initial optimized results with the use of a GA.

Table 5.3: Optimal parameters, T_0, λ_0, P_0, obtained for spectral tuning in the zoom-in stage optimization by exhaustive search with $m = 675$. The soliton order, N, fitness value, ϕ, output central wavelength, λ_c, and efficiency of frequency conversion, η, are shown as the obtained results.

Optimal parameters			Results			
T_0 (fs)	λ_0 (nm)	P_0 (kW)	N	ϕ $(10^{-4}/W)$	λ_c (nm)	$\eta(\%)$
93	814	10.06	46.54	1.296	1025	19.46
98	812	10.12	52.98	0.953	1075	23.83
101	847	6.92	22.79	1.289	1125	21.43
88	833	10.27	28.88	1.212	1175	19.45
97	850	8.84	23.48	0.992	1225	22.46
103	850	12.25	29.65	0.908	1275	20.45
103	850	13.82	31.86	1.413	1325	19.34
108	850	14.78	31.69	1.098	1375	22.54

5.3 Dual-pulse solitonic source optimization

The same numerical strategy is used to design fiber based dual pulse light sources exhibiting two predefined spectral peaks in the anomalous group velocity dispersion regime. The frequency conversion is based on the soliton fission and soliton self-frequency shift occurring during supercontinuum generation. Such spectra were important for applications in optical coherence tomography (OCT) with wavelengths in the near infra-red (NIR) window [26, 27, 30]: $\lambda \lesssim 1$ μm.

To demonstrate the usefulness of this method, it is considered the two spectral channels separated by 100 nm (see, e.g., Ref. [34]). The optimization method finds the same optimal input pulse parameters of the section 5.2, namely central wavelength, λ_0, temporal width, T_0, and peak power, P_0, yielding the desired spectra. The obtained peak powers are of up to 90 mW for each spectral band, satisfying the needs for OCT imaging applications [38]. This method finds the possibility to tune the wavelength of the target spectral channels, which represents an important feature of this strategy since the greatest potential of the given PCF is exploited, specially in situations where limited choice of PCF designs is

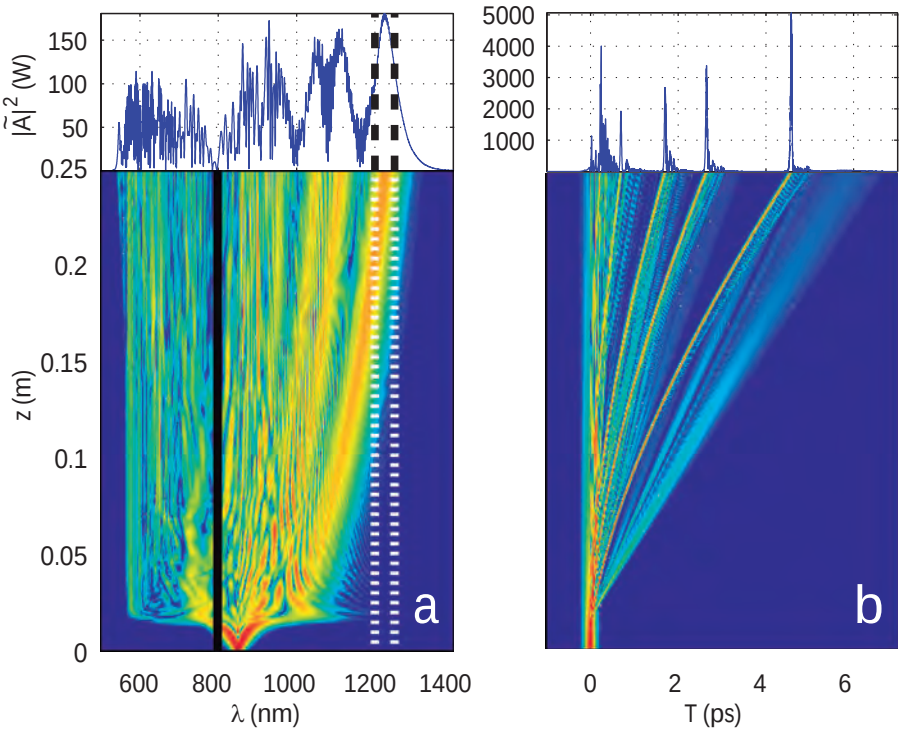

Figure 5.4: Spectral (a) and temporal (b) window evolution on distance z corresponding to optimized parameters $T_0 = 97$ fs, $\lambda_0 = 852$ nm and $P_0 = 8.84$ kW for a channel centred in $\lambda_c = 1225$ nm corresponding to zoom-in of optimal solutions (as in Table 5.3). In the spectral window, white dashed vertical lines shows the channel spectrum with maximum spectral power obtained by the GA and the continuous black vertical line represent the *zero GVD*.

available.

For each simulation along the PCF, the GA generates an *individual* with the *genome* $\mid g\rangle \equiv [g_1, g_2, g_3]^T = [T_0, \lambda_0, P_0]^T$ and evaluates how suitable that individual is from the simulation output through the new *fitness* function (to be minimized) defined as

$$\phi_2 \equiv \psi_1^{-1} \cdot \psi_2^{-1}, \qquad \psi_j(\omega_{c_j}; \Delta\omega) \equiv \int_{\omega_{c_j}-\Delta\omega}^{\omega_{c_j}+\Delta\omega} d\omega' |\tilde{A}(L, \omega')|^2, \qquad j = 1, 2, \quad (5.4)$$

where $2\Delta\omega$ is the chosen spectral channel widths and $\omega_{c_j} = 2\pi c/\lambda_{c_j}$ the central frequency. Note that the definition of ϕ_2 as a product tends to favor output spectra in the form $\psi_1 \approx \psi_2$ amongst all solutions with $\psi_1 + \psi_2 = const$.

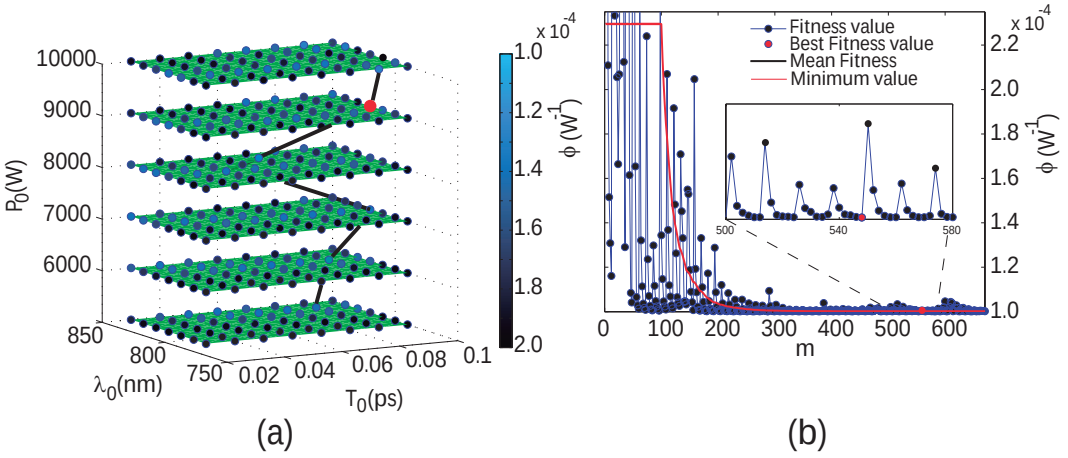

Figure 5.5: (a) Fitness value charts for different P_0 values with $m = 675$ generated by GRID for $\lambda_c = 1225$ nm without the use of the GA. The color of the points shows the fitness (ϕ) value of each individual, lighter points have smaller ϕ (thus, better fitness values) and the optimal individual is represented as the red point sited in the coordinates of the three optimized parameters. The black polygonal-line sorts the best individuals for the specific P_0. (b) Fitness value evolution of executions in chronological order of generation during the optimization procedure with the minimum global value (red line). The *sawtooth* beehavior of the fitness value evolution is shown in the inset.

Figure 5.6 shows the spectral evolutions (bottom) and output spectrograms (top) corresponding to the best individuals obtained by the GA strategy and fitness function of Eq. 5.4. All output spectra shown in Fig. 5.6 present the two reddest solitonic pulses, ejected from the soliton fission, accurately centered in the predefined channels ($\lambda_{c_{1,2}}$) delimited by the dashed lines (see Table 5.4 for parameter values associated to results in Fig. 5.6). In Figs. 5.6(a) and 5.6(d), the target spectral channels where chosen from Ref. [34] in order to illustrate the solution for a dual-pulse source required in a realistic application. The other two cases, Figs. 5.6(b,e) and Figs. 5.6(c,f), demonstrate the tunability of such source, keeping $\lambda_{c_1} - \lambda_{c_2}$ fixed to 100 nm without replacing the PCF but merely adjusting the input pulse parameters. We checked by benchmarks that several runs of the GA with fixed $\lambda_{c_{1,2}}$ provided systematically very similar optimal results and therefore only one is shown here for each different case.

Regarding OCT applications, another important aspect of the source pre-

sented here is that the fs-SC dynamics typically exhibits a very high coherence and negligible shot-to-shot fluctuations [3], known to be detrimental for OCT [38]. Moreover, the two output solitonic pulses ($S_{1,2}$ in Fig. 5.6) constituting the proposed OCT light source, provide a decent resolution $l_c \equiv 2\ln 2\lambda_s/[\pi\Delta\lambda_{s,FWHM}]$ [42] of ~ 10 μm for the two solitons, $S_{1,2}$.

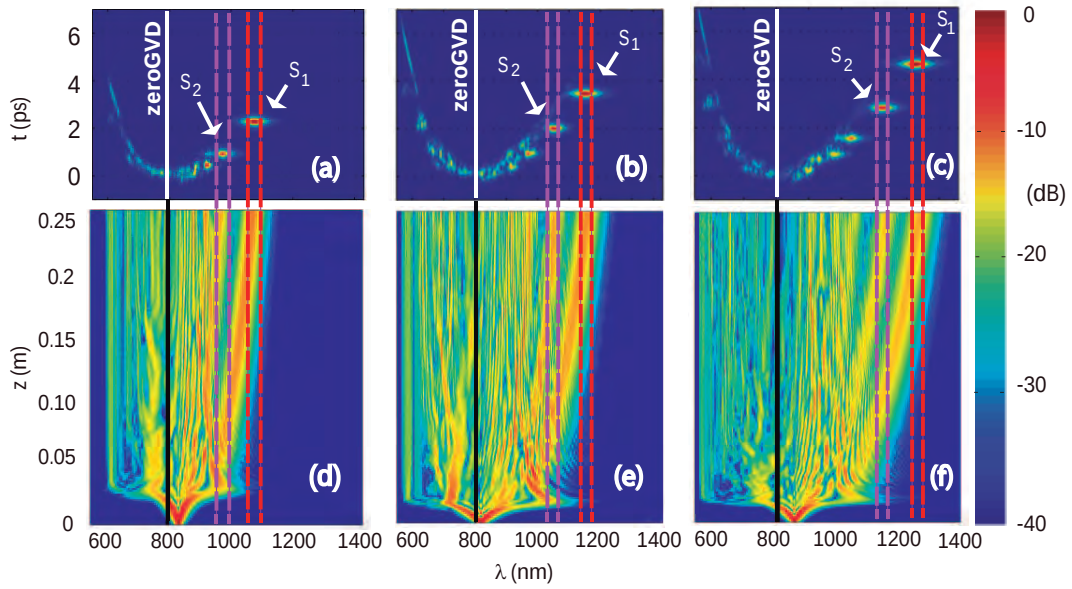

Figure 5.6: (a-c) Spectrograms of the output spectra at $z = 25$ cm, corresponding to the optimization results given by the GA algorithm after $m = 300$ evaluations. $S_{1,2}$ label the two solitonic pulses. (d-f) Spectral evolutions along the fiber associated to (a-c), respectively, retrieved from the optimal input pulse parameters corresponding to three different pairs of channels, $\lambda_{c_{1,2}}$. Input pulse parameters are given in Table 5.4. Vertical solid lines mark the zero GVD wavelength.

Figure 5.7(a) shows the $3D$ chart in the parameter space containing all 300 individuals involved in the optimization process. Data points distributed all over the volume are typically generated by the random stage 1 ($m < p_{th} = 50$) and GOs tend to accumulate solutions around small volumes where fitness is typically small, with the overall effect of monotonically decreasing the average fitness value, observed when fitness is represented in order of execution [black curve in Fig. 5.7(b)]. However, the scattering ability of GAs often results in finding

Table 5.4: Parameters associated to the best individuals found by the GA, shown in Fig. 5.6.

Optimal pulse parameters				Spectral bands	Resolution	Fitness	Shown in
T_0 (fs)	λ_0 (nm)	P_0 (kW)	N	λc_1, λc_2 (nm)	l_{c_1}, l_{c_2} (μm)	ϕ_2 ($10^{-4}/W$)	
90.01	834.98	5.012	20.14	1075, 975	9.8, 9.5	1.138	Figs. 5.6(a,d)
70.80	817.27	12.3501	36.24	1150, 1050	10.6, 9.2	1.107	Figs. 5.6(b,e)
101.13	849.24	9.6617	26.43	1225, 1125	10.1, 10.1	1.018	Figs. 5.6(c,f)

slightly better individuals in nearby regions presenting smaller agglomeration. An important reason for the convergence of our GA towards the optimal solutions is the fact that the operator $\hat{\mathcal{M}}$ is given a lower probability of action than $\hat{\mathcal{X}}$ (probabilities are 1/3 and 0.95 respectively, see section 2.2). This combination gives both a good diversity and probability to conserve the properties of the best individuals during the execution of the GA.

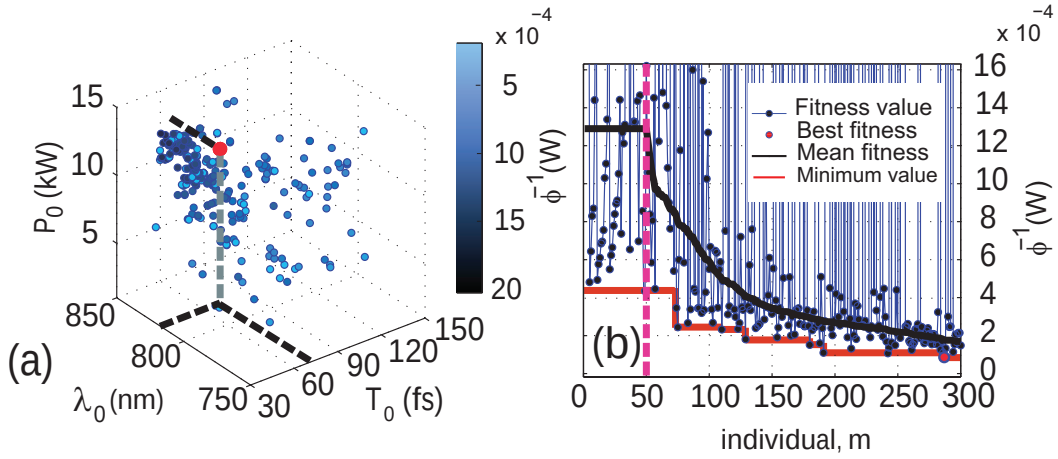

Figure 5.7: (a) Parameter space cloud of the 300 individuals (and fitness) generated by the GA in the optimization yielding to the solution in Figs. 5.6 (b),(e). The best individual is marked in red and dashed mark its input parameters. (b) Fitness evolution versus generated individuals in chronological order. Dashed vertical line marks the threshold population $p_{th} = 50$ corresponding to the end of stage 1 (random generation). Best (at $m \approx 260$), Instantaneous minimum, and average fitness are also plotted (see legend).

References

[1] J. P. Gordon, *"Theory of the soliton self-frequency shift,"* Opt. Lett. **11,** 662–664 (1986). 57, 64

[2] F. M. Mitschke and L. F. Mollenauer, *"Discovery of the soliton self-frequency shift,"* Opt. Lett. **11,** 659–661 (1986). 57

[3] J. M. Dudley, G. Genty and S. Coen, *"Supercontinuum generation in photonic cristal fibers,"* Rev. Mod. Phys. **78,** 135–1184 (2006). 57, 70

[4] D. V. Skryabin and A. V. Gorbach, *"Colloquium: looking at a soliton through the prism of optical supercontinuum,"* Rev. Mod. Phys. **82,** 1287–1299 (2010). 57

[5] A. V. Gorbach and D. V. Skryabin, *"Light trapping in gravity-like potentials and expansion of supercontinuum spectra in photonic-crystal fibres,"* Nat. Photon. **1,** 1749-4885 (2007). 57

[6] A. Hause, T. X. Tran, F. Biancalana, A. Podlipensky, P. St.J. Russell and F. Mitschke, *"Understanding Raman-shifting multipeak states in photonic crystal fibers: two convergent approaches,"* Opt. Lett. **35,** 2167–2169 (2010). 57

[7] A. Hause and F. Mitschke, *"Soliton trains in motion,"* Phys. Rev. A **82,** 043838 (2010). 57

[8] T. X. Tran, A. Podlipensky, P. St. J. Russell and F. Biancalana, *"Theory of Raman multipeak states in solid-core photonic crystal fibers,"* J. Opt. Soc. Am. B **27,** 1785–1791 (2010). 57

[9] Andrey V. Gorbach and Dmitry V. Skryabin, *"Soliton self-frequency shift, non-solitonic radiation and self-induced transparency in air-core fibers,"* Opt. Express **16,** 4858–4865 (2008). 57

[10] C. Milián, D. V. Skryabin and A. Ferrando, *"Continuum generation by dark solitons,"* Opt. Lett. **34,** 2096–2098 (2009). 57

[11] C. Milián, A. Ferrando, and D. V. Skryabin, *"Polychromatic Cherenkov radiation and supercontinuum in tapered optical fibers,"* J. Opt. Soc. Am. B **29,** 589-593 (2012). 57

[12] S. A. Dekker, A. C. Judge, R. Pant, I. Gris-Sánchez, J. C. Knight, C. M. De Sterke and B. J. Eggleton, *"Highly-efficient, octave spanning soliton self-frequency shift using a specialized photonic crystal fiber with low OH loss,"* Opt. Express **18,** 17766–17773 (2011). 57

[13] J. Rothhardt, A. M. Heidt, S. Hädrich, S. Demmler, J. Limpert and A. Tünnermann, *"High stability soliton frequency-shifting mechanisms for laser synchronization applications,"* J. Opt. Soc. Am. B **29,** 1257–1262 (2012). 57

[14] A. M. Al-kadry and M. Rochette, *"Mid-infrared sources based on the soliton self-frequency shift,"* J. Opt. Soc. Am. B **29,** 1347–1355 (2012). 57

[15] A. C. Judge, O. Bang, B. J. Eggleton, B. T. Kuhlmey, E. C. Mägi, R. Pant and C. Martijn de Sterke, *"Optimization of the soliton self-frequency shift in a tapered photonic crystal fiber,"* J. Opt. Soc. Am. B **26,** 2064–2071 (2009). 57

[16] S. Pricking and H. Giessen, *"Tailoring the soliton and supercontinuum dynamics by engineering the profile of tapered fibers,"* Opt. Express **18,** 20151–20163 (2010). 57

[17] R. Pant, A. C. Judge, E. C. Magi, B. T. Kuhlmey, M. De Sterke and B. J. Eggleton, *"Characterization and optimization of photonic crystal fibers for enhanced soliton self-frequency shift,"* J. Opt. Soc. Am. B **27,** 1894–1901 (2010). 57

[18] P. F. Moulton, *"Spectroscopic and laser characteristics of Ti:Al2O3,"* J. Opt. Soc. B **3,** 125 (1986). 58

[19] G. Moltó, M. Arevalillo-Herráez, C. Milián, M. Zacarés, V. Hernández, and A. Ferrando, *"Optimization of supercontinuum spectrum using genetic algorithms on service-oriented grids,"* in *Proceedings of the 3rd Iberian Grid Infrastructure Conference* (IberGrid), pp. 137–147 (2009). 58

[20] A. Ferrando, C. Milián, N. González, G. Moltó, P. Loza, M. Arevalillo-Herráez, M. Zacarés, I. Torres-Gómez and V. Hernández, *"Designing supercontinuum spectra using Grid technology,"* Proc. SPIE **7839,** 78390W (2010). 58

[21] E. Kerrinckx, L. Bigot, M. Douay and Y. Quiquempois, *"Photonic crystal fiber design by means of a genetic algorithm,"* Opt. Express **12,** pp. 1990–1995 (2004). 58

[22] W. Q. Zhang, J. E. Sharping, R. T. White, T. M. Monro and S. Afshar V., *"Design and optimization of fiber optical parametric oscillators for femtosecond pulse generation,"* Opt. Express **18,** 17294–17305 (2010). 58

[23] W. Q. Zhang, S. Afshar V. and T. M. Monro, *"A genetic algorithm based approach to fiber design for high coherence and large bandwidth supercontinuum generation,"* Opt. Express **17,** 19311–19327 (2009). 58

[24] R. R. Musin and A. M. Zheltikov, *"Designing dispersion-compensating photonic-crystal fibers using a genetic algorithm,"* Opt. Commun. **281,** 567–572 (2008). 58

[25] Y. Guo-Bing, L. Shu-Guang, L. Shuo and W. Xiao-Yan, *"The Optimization of Dispersion Properties of Photonic Crystal Fibers Using a Real-Coded Genetic Algorithm,"* Chinese Phys. Lett. **28,** 064215 (2011). 58

[26] J. Wang, Y. J. Geng, B. Guo, T. Klima, B. N. Lal, J. T Willerson and W. Casscells, *"Near-infrared spectroscopic characterization of human advanced atherosclerotic plaques,"* J. Am. Coll. Cardiol. **39,** 1305-1313 (2002). 58, 67

[27] Y. M. Wang, J. S. Nelson, Z. P. Chen, B. J. Reiser, R. S Chuck and R. S. Windeler, *"Optimal wavelength for ultrahigh-resolution optical coherence tomography,"* Opt. Express **11,** 1411-1417 (2003). 58, 67

[28] J. G. Fujimoto, *"Optical coherence tomography for ultrahigh resolution in vivo imaging,"* Nat. Biotechnol. **21,** 1361–1367 (2003). 4, 58

[29] A, Unterhuber, B. Povazay, K. Bizheva, B. Hermann, H. Sattmann, A. Stingl, T. Le, M. Seefeld, R. Menzel, M. Preusser, H. Budka, C. Schubert, H. Reitsamer, P.K. Ahnelt, J.E. Morgan, A. Cowey and W. Drexler, *"Advances in broad bandwidth light sources for ultrahigh resolution optical coherence tomography,"* Phys. Med. Biol. **49,** 1235-1246 (2004). 58

[30] G, Humbert, W. J. Wadsworth, S. G. Leon-Saval, J. C. Knight, T. A. Birks, P. St. J. Russell, M. J. Lederer, D. Kopf K. Wiesauer, E. I. Breuer and D. Stifter, *"Supercontinuum generation system for optical coherence tomography based on tapered photonic crystal fibre,"* Opt. Express **14,** 1596-1603 (2006). 58, 67

[31] F. Spoeler, S. Kray, P. Grychtol, B. Hermes, J. Bornemann, M. Foerst and H. Kurz, *"Simultaneous dual-band ultra-high resolution optical coherence tomography,"* Opt. Express **15,** 10832-10841 (2007). 58

[32] S. Ishida and N. Nishizawa, *"Quantitative comparison of contrast and imaging depth of ultrahigh-resolution optical coherence tomography images in 800-1700 nm wavelength region,"* Biomed. Opt. Express **3,** 282-294 (2012). 58

[33] A.M. Smith, M.C. Mancini, and S. Nie, *"Bioimaging: Second window for in vivo imaging,"* Nat. Nanotechnol. **4,** 710-711 (2009). 58

[34] Q. Cao, N.G. Zhegalova, S.T. Wang, W.J. Akers, and M.Y. Berezin, *"Multi-spectral imaging in the extended near-infrared window based on endogenous chromophores,"* J. Biomed. Opt. **18,** 101318–101318 (2013). 58, 67, 69

[35] S. Afshar V. and T. M. Monro, *"A full vectorial model for pulse propagation in emerging waveguides with subwavelength structures part I: Kerr nonlinearity,"* Opt. Express **17,** 2298–2318 (2009). 59

[36] R. H. Stolen, J. P. Gordon, W. J. Tomlinson and H. A. Haus, *"Raman response function of silica-core fibers,"* J. Opt. Soc. Am. B **6,** 1159–1166 (1989). 59

[37] Y. Wang, Y. Zhao, J. S. Nelson, Z. Chen, R. S. Windeler, *"Ultrahigh-resolution optical coherence tomography by broadband continuum generation from a photonic crystal fiber,"* Opt. Lett. **28,** 182–184 (2003). 61

[38] J.G. Fujimoto, C. Pitris, S. A. Boppart and M.E, Brezinski, *"Optical coherence tomography: An emerging technology for biomedical imaging and optical biopsy,"* Neoplasia **2,** 9-25 (2000). 61, 67, 70

[39] A.N. Bashkatov1, E.A. Genina, V.I. Kochubey, and V.V. Tuchin, *"Optical properties of human skin, subcutaneous and mucous tissues in the wavelength range from 400 to 2000 nm,"* J. Phys. D: Appl. Phys. **38,** 2543–2555 (2005). 61

[40] R. Tripathi, N. Nassif, J. S. Nelson, B. H. Park and J. F. de Boer, *"Spectral shaping for non-Gaussian source spectra in optical coherence tomography,"* Opt. Lett. **27,** 406–408 (2002). 61

[41] Y. Kodama and A. Hasegawa, *"Nonlinear Pulse Propagation in a Monomode Dielectric Guide,"* IEEE J. Quantum Elect. **23,** 510-524 (1987). 63

[42] J. A. Izatt and M. A. Choma, *Optical Coherence Tomography Technology and Applications* (Springer, 2008). 70

6

Ultra-flat spectrum by optimizing the zero dispersion wavelength profile using GAs

The SPM is a well-known effect that induce spectral broadening in optical fibers [1, 2] and it has been used successfully to obtain flat and ultra flat spectra by both, input-pulse shaping [3, 4] and the use of specially designed tapered microstructured optical fibers [5, 6, 7].

In this chapter, we propose a technique of spectral modelling using a laser source with a pulse in the form of Eq. 2.4 with fixed pulse commercial parameters, namely input wavelength $\lambda_0 = 1270$ nm, temporal width $T_0 \equiv T(z=0) \equiv T_{FWHM}/2\ln[1+\sqrt{2}] \approx 28.4$ fs and peak power $P_0 = 7$ kW, pumped in a standard single mode fiber (SMF), which its zero dispersion wavelength (λ_{ZDW}) profile has been designed under a fitness function criteria and genetic algorithm (GA) optimization. The suit of λ_{ZDW} and the management of the nonlinear coefficient γ can be achieved by an appropriate tapering of standard optical fiber or structural parameters (see section 2.2). Some studies are dedicated to change the λ_{ZDW} by tapered fibers [8, 9, 10], or by immersing the fibers in different liquids [11]. Moreover, the control of fiber taper shape has been studied by heat stretching [12], or reducing their cladding diameter by using chemical etching methods that achieve submicron-diameters [13]. We planted the search of external parameters (see section 2.2)to linearly change the λ_{ZDW} across the fiber length in roder to obtain an

ultra-flat spectral output centred in $\lambda_c = 1285$ nm. The 1285 nm wavelength is an important frequency for a variety of applications, for example, in some kind of OCT imaging devices, the 1285 nm wavelength system has an important advantage over the shorter wavelength ones due to the fact that tissue scattering decreases with wavelength [14]. Moreover, one of the most important applications of ultra-flat continuum is in the field of optical telecommunications, the design of multi-wavelength sources for wavelength division multiplexing (WDM) transmission systems based on spectral slicing of this one by an optical demulteplexing [15].

6.1 Pulse propagation and fitness function

Using a Fourier split-step method (see section 2.1.1), we simulate the propagation of optical pulses with complex amplitude $A(z,t)$ in a tapered SMF by integrating numerically the Eq. 2.2, where the dispersion coefficients $\beta_q(z)$'s (up to $q = 10$ in this work) account for the linear fiber dispersion $D(z)$ at the pump frequency $\omega_0 = 2\pi c/\lambda_0$ ($\lambda_0 = 1270$ nm). The β_2 coefficient is related to λ_{ZDW} by the dispersion $-2\pi c\beta_2/\lambda_{ZDW}^2 = 0$. Nonlinearity is included through the parameter $\gamma(z)$ and the response function $R(T) \equiv [1 - f_R]\delta(T) + f_R h_R(T)\Pi(T)$, where $f_R = 0.18$, h_R is the commonly used Raman response of silica [16], and $\delta(T)$, $\Pi(T)$ are the Dirac, Heaviside functions, respectively. The nonlinear coefficient, $\gamma(z)$, and dispersion parameter $D(z)$ associated to $\beta_q(z)$ (where z depends on the tapered fiber diameter d), were computed using Optiwave [17] for different diameters of the SMF (see Fig.6.1). The position of the λ_{zGVD} along propagation requires to have a fine control of the taper. From our numerical data of dispersion, it is possible to find a convenient fit to link it with the SMF cladding diameter, d (see Fig. 6.1(c)):

The input pulse used in this work is of the form $A(z = 0, t) = \sqrt{P_0}\,\mathrm{sech}(t/T_0)$ with intensity full width at half maximum $T_{FWHM} = 50$ fs ($T_0 \approx 28.4$) and the peak power (P_0) of 7000 W. The soliton order N is computed by Eq. 2.8.

The GA individuals are the result of the evaluation of a set of external parameters (initial and final λ_{ZDW}, i.e. λ_{ZDW_0} and λ_{ZDW_L} respectively, and propagation

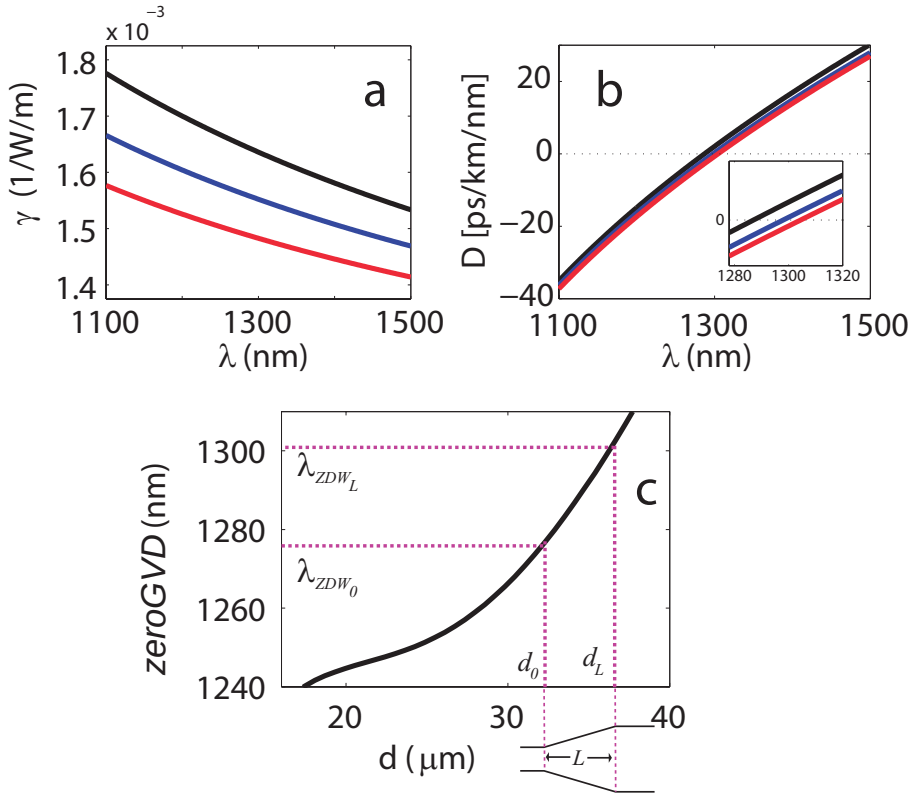

Figure 6.1: (a) Nonlinear coefficient γ and (b) dispersion parameter D for different cladding diameters: $d = 34.1, 36.6$ and 37.2 μm (black, blue and red respectively). (c) Dependence of $zeroGVD$ on the SMF diameter d. Down scheme shows the side view of the resultant linear tapered fiber, in which light propagation occurs from left to right. The optimized taper length is $L = 7.6$ cm, and the diameters are $d_0 = 32.4$ and $d_L = 37.8$ μm.

length L in this work) and applies a minimization strategy to find the solutions taking the minimum values of the fitness function ϕ.

At the end (after $m = 300$ in our case), the best individual is picked of the evolved population and chosen as optimal solution (see Fig 6.2).

6.2 Ultra-flat spectrum

We implemented an optimization of three generations with a total of $m = 300$ individuals. The GA is designed to find the minimum value of the fitness function

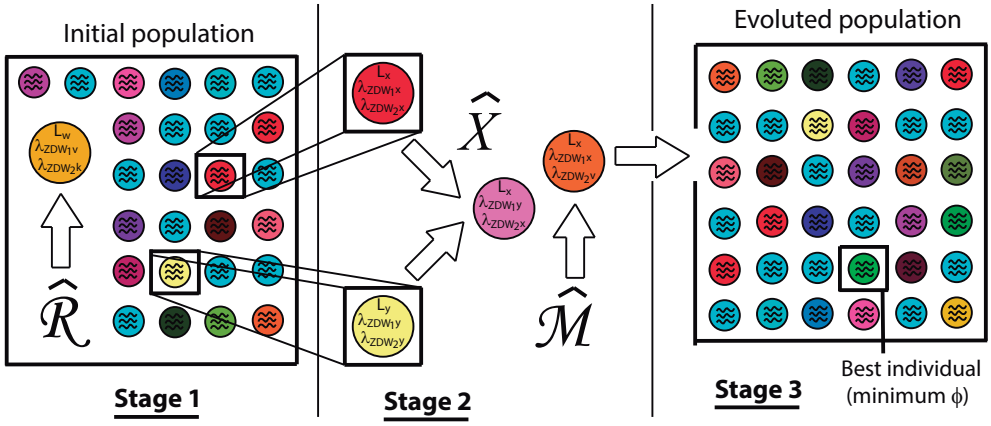

Figure 6.2: Diagram of the operation of the GA. In first stage a population of possible solutions is generated randomly. In the second stage, new individuals are created by $\hat{\mathcal{M}}$, $\hat{\mathcal{X}}$ or $\hat{\mathcal{R}}$ and each one is compared with the worst solution created in the initial population, if the new individual is better, then it is selected as a new individual in the next generation instead the worst solution, otherwise is dismissed.

ϕ that depends on the three λ_{ZDW}-profile parameters (λ_{ZDW_0}, λ_{ZDW_L}, and L). The fitness function ϕ is defined as the area limited by spectral output in the bottom, since $\lambda_{min} = 1270$ nm to $\lambda_{max} = 1310$ nm and a reference A_{ref} in the top, the last being the maximum value of $A^2(z = L, \lambda)$ (see Fig. 6.3(a)),

$$\phi(\lambda_{ZDW_0}, \lambda_{ZDW_L}, L) = \int_{\lambda_{min}}^{\lambda_{max}} [A_{ref} - |A|^2(z = L, \lambda)] d\lambda. \tag{6.1}$$

Due to the function fitness characteristics, the GA will find the set of parameters that make $\phi = 0$ (ideal solution). If the desired shape can not be achieved (limited by the effect of optimized parameters on interplay of nonlinear effects), the GA will find the closest value, it is related to the closest shape to the desired one. We make λ_{ZDW_0} and λ_{ZDW_L} vary in the range of $[1270, 1310]$ nm to ensure the pump in the normal region of the system and acquire relevant SPM effects, whereas L is changed in the interval of $[5, 10]$ cm. In this particular optimization problem, each evaluation typically requires 8 min in a conventional 12 Gb-RAM computer system, which is equivalent to ~ 40 hr of CPU time to perform a single run over $m = 300$ individuals.

The GA convergence is shown in fig. 6.3(b). A significant improvement in

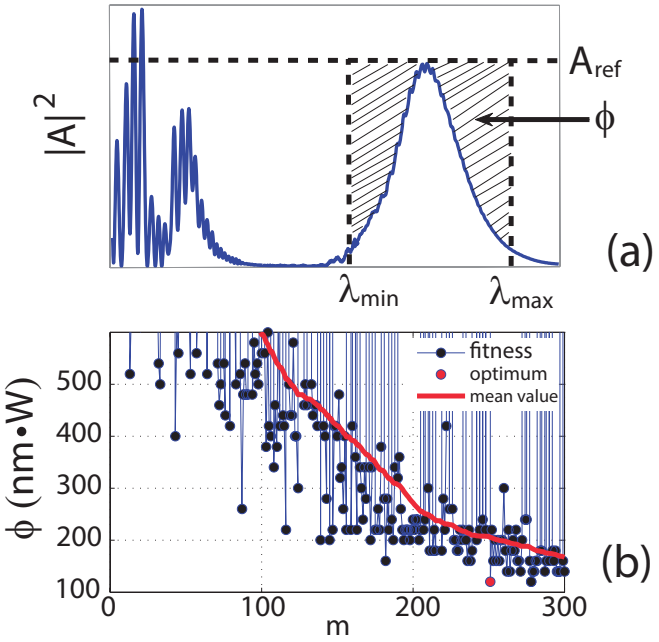

Figure 6.3: (a) Schematic description of the fitness function definition. The shaded area defines the value of the fitness function ϕ. (b) Fitness function value evolution during the GA optimization.

the fitness function value of the population is apparent, the mean fitness function value of the population (red line) is monotonically decreasing as new individuals are generated.

The best individual within the final population is taken as the optimized value. The optimized parameters, result of the mentioned conditions, are shown in Table 6.1. According to Fig.6.1(c), we obtain a linear-tapered fiber, which initial and final diameters are $d_0 = 32.3$ and $d_L = 37.8$ μm respectively.

Table 6.1: Optimal parameters, λ_{ZDW_0}, λ_{ZDW_L}, L, obtained for ultra-flat spectra by the GA optimization with $m = 300$. The fixed laser parameters T_{FWHM}, λ_0, P_0, with the fitness function value $\phi = 114.11$ are shown.

Pulse parameters			Optimal taper parameters		
T_{FWHM} (fs)	λ_0 (nm)	P_0 (W)	L (cm)	λ_{ZDW_0} (nm)	λ_{ZDW_L} (nm)
50	1270	7000	7.6	1277	1302

Figure 6.4 shows spectral and temporal evolution of an $N(z=0) \approx 3.24$ pulse at the optimized length $L = 7.6$ cm. The black continuous line represents the optimized λ_{GVD} and the white dashed lines delimit the spectral channel where the ultra-flat spectral power was defined. Here it is shown the obtained flat-spectrum exhibiting a 1-dB bandwidth of 90 nm and a 0.5-dB bandwidth of 50 nm.

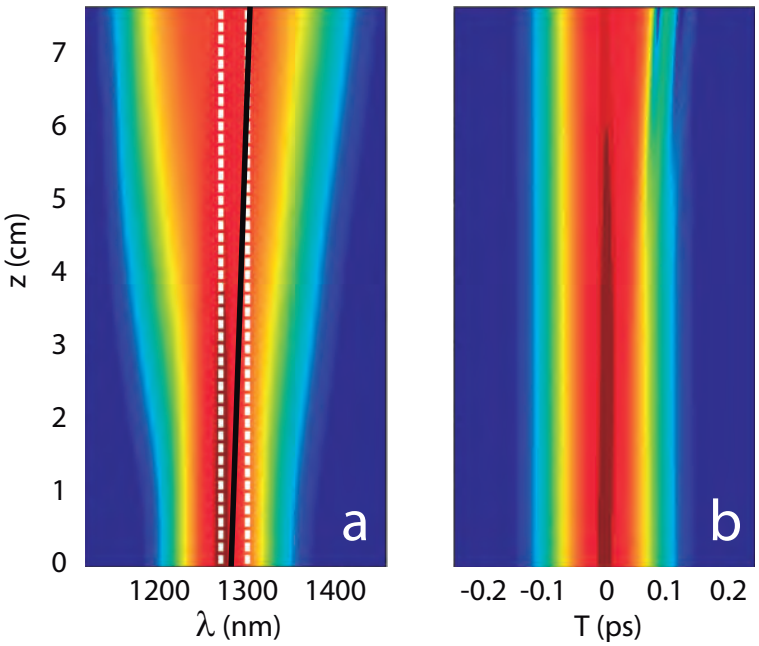

Figure 6.4: (a) Spectral and (b) temporal evolution of a tapered SMF of optimized $L = 7.6$ cm with $\lambda_{ZDW_0} = 1267$ nm and $\lambda_{ZDW_L} = 1302$ nm. It is pumped with a fixed sech pulse centred in $\lambda = 1270$ nm with 7000 W of peak power and a temporal width of 50 fs (FWHM). Dashed vertical lines shows the spectral channel and the continuous black vertical line represent the λ_{ZDW}.

The SPM has been demonstrated to be a crucial process in the initial stage of the SC generation [16]. As we can see in the Fig. 6.4(b), a temporal compression on the pulse is occurring, and it is directly associated with a relatively uniform broadening on the spectral behavior in 6.4(a), it is certainly characteristic effects of SPM. Although, nonlinear effects start their influence on the process (nonlinear length, $L_{nl} \sim 7.15$ cm), another effects like four wave mixing (FWM) and soliton fission can acquire relevant importance both in the spectral broadening and its shape, but due to the constant increase in $|\beta_2(z, \omega_0)|$ and the decrease in the

nonlinearity coefficient $\gamma(z, \omega_0)$ (both caused by the increase of the fiber diameter across the propagation direction), these effects gradually decrease their impact on the entire process. Finally, Fig. 6.5 shows the spectral output, both in linear and logarithm scale, where the ultra-flat spectrum in the 1-dB power bandwidth is shown.

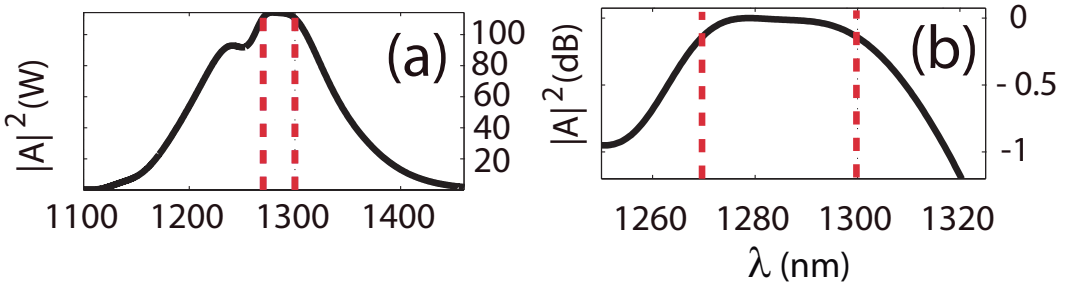

Figure 6.5: (a) Ultra-flat spectral output in linear scale of a sech pulse tapered SMF centred in $\lambda = 1270$ nm, with 7000 W of peak power and a temporal width of 50 fs (FWHM), in a optimized $L = 7.6$ cm with $\lambda_{ZDW_0} = 1267$ and $\lambda_{ZDW_L} = 1302$ nm. Dashed vertical lines shows the defined spectral channel. (b) The 1-dB power bandwidth is shown in logarithm scale.

We have demonstrated the use of GAs as a tool to get well-shaped spectral outputs that can be useful for a variety of applications. Our strategy consists in using a conventional tapered SMF, a laser source with commercial fixed parameters, and the well-defined fitness function to find the spectral output that best suits to a pre-defined shape. In this work, we have obtained optimized fiber parameters that can be suited with a taper, but it is possible to optimize the laser source parameters as well, in order to not change the dimensions of the propagation medium.

6. ULTRA-FLAT SPECTRUM BY OPTIMIZING THE ZERO DISPERSION WAVELENGTH PROFILE USING GAS

References

[1] R. H. Stolen and C. Lin, *"Self-phase-modulation in silica optical fibers,"* Phys.Rev. A **17,** 1448 (1978). 79

[2] O. Boyraz, T. Indukuri, and B. Jalali, *"Self-phase-modulation induced spectral broadening in silicon waveguides,"* Opt. Express **12,** 829-834 (2004). 79

[3] X. Yang, D. J. Richardson, and P. Petropoulos, *"Nonlinear Generation of Ultra-Flat Broadened Spectrum Based on Adaptive Pulse Shaping,"* J. Lightwave Technol. **30,** 1971-1977 (2012). 79

[4] K. Kashiwagi, H. Ishizu, Y. Kodama, and T. Kurokawa, *"Background suppression in synthesized pulse waveform by feedback control optimization for flatly broadened supercontinuum generation,"* Opt. Express **21,** 3001-3009 (2013). 79

[5] R. Buczynski, D. Pysz, T. Martynkien, D. Lorenc, I. Kujawa, T. Nasilowski, F. Berghmans, H. Thienpont, and R. Stepien, *"Ultra flat supercontinuum generation in silicate dual core microstructured fiber,"* Laser Phys. Lett. **6,** 575-581 (2009). 79

[6] N. Vukovic and N. G. R. Broderick, *"Method for improving the spectral flatness of the supercontinuum at 1.55 μm in tapered microstructured optical fibers,"* Phys. Rev. A **82,** 043840 (2010). 79

[7] L. E. Hooper, P. J. Mosley, A. C. Muir, W. J. Wadsworth, and J. C. Knight, *"Coherent supercontinuum generation in photonic crystal fiber with all-normal group velocity dispersion,"* Opt. Express **19,** 4902-4907 (2011). 79

[8] W. J. Wadsworth, A. Ortigosa-Blanch, J. C. Knight, T. A. Birks, T.-P. Martin Man, and P. St. J. Russell, *"Supercontinuum generation in photonic crystal fibers and optical fiber tapers: a novel light source,"* J. Opt. Soc. Am. B **19,** 2148-2155 (2002). 79

[9] R. Zhang, X. Zhang, D. Meiser, and H. Giessen, *"Mode and group velocity dispersion evolution in the tapered region of a single-mode tapered fiber,"* Opt. Express **12,** pp. 5840-5849 (2004). 79

[10] A. Kudlinski, A. K. George and J. C. Knight, *"Zero-dispersion wavelength decreasing photonic crystal fibers for ultraviolet-extended supercontinuum generation,"* Opt. Express **14,** 5715-5722 (2006). 79

[11] R. Zhang, J. Teipel, X. Zhang, D. Nau, and H. Giessen, *"Group velocity dispersion of tapered fibers immersed in different liquids,"* Opt. Express **12,** pp. 1700-1707 (2004). 79

[12] R.P Kenny, T.A. Birks, and K.P. Oakley, *"Control of optical fibre taper shape,"* Electron. Lett. **27,** pp. 1654-1656 (1991). 79

[13] H.J. Kbashi, *"Fabrication of Submicron-Diameter and Taper Fibers Using Chemical Etching,"* J. Mater. Sci. Technol. **28,** 308 - 312 (2012). 79

[14] Y. Pan and D. L. Farkas, *"Noninvasive imaging of living human skin with dual-wavelength optical coherence tomography in two and three dimensions,"* J Biomed Opt. **3,** 446-455 (1998). 80

[15] L. Graini and K. Saouchi , *"WDM Transmitter Based on Spectral Slicing of Similariton Spectrum,"* Lecture Notes on Photonics and Optoelectronics **1,** 30-34 (2013). 80

[16] G. P. Agrawal, *Nonlinear Fiber Optics, 4th ed.* (Academic Press. 2007). 80, 84

[17] www.optiwave.com 80

7

Conclusions

Throughout the development of this work, it has been shown that it is possible to model the spectral output of the supercontinuum (SC) generation by both physical-mathematical analysis and by the use of computational tools such as genetic algorithms and GRID infrastructure. Firstly and regarding the physical-mathematical analysis, it has been presented a versatile method to obtain a multi-peak spectra exhibiting predefined discrete peaks arising from IR Cherenkov radiation emitted from bright solitons. This mechanism is based on an on/off switch made by splicing several pieces of uniform single mode fiber (SMF) and pumping with a commercial micro-chip laser at 1060 nm. This is motivated by the wide interest that the second near IR window (950-1350 nm) presents for medical imaging. This device can be efficiently controlled by the adequate design of the group velocity dispersion (GVD) profiles of each fiber segment, being the zero dispersion wavelength, λ_{zGVD}, the key parameter to control. Our numerical results show the generation of well defined spectral peaks when we launch solitonic pulses in a non-uniform fiber consisting on several uniform sections, each of them with different cladding diameters. These diameters can be selected in order to obtain highly efficient energy transfer between the soliton and the dispersive waves (DWs) at selected wavelengths. Additionally, strong remnants of Airy waves also grow in the spectrum which may constitute an interesting extra degree of freedom to control the spectral profile. Our analysis demonstrates that a single soliton ($N < 2$) is enough to efficiently generate several spectral peaks

from dispersive waves. This method is versatile for applications requiring the simultaneous illumination with light containing multiple and specific wavelengths and can be implemented using off-the-shelf optic components such as a standard SMFs and common laser sources.

Secondly and regarding computational tools, it is presented a well defined and efficient optimization procedure of a Ti:Saphire laser pulse parameters to obtain the maximum frequency conversion using a simple device by mean of SC generation in the anomalous region. Unlike the previous optimization method, this optimization is achieved with the use of genetic algorithms (GAs) and GRID infrastructure. Therefore, it has been shown that efficient spectral conversion based on soliton self-frequency shift (SSFS) can be achieved using a simple photonic crystal fiber (PCF) as a medium of generating spectral broadening pumped by a Ti:Sapphire laser just by properly controlling optimized input pulses. Since the optimization algorithm has been properly encoded for its deployment into a GRID platform, scalability of the optimization procedure is guaranteed if required. This scenario involves fission into multisoliton states that provide different spectral channels for frequency conversion, thus, decreasing the conversion efficiency into every single channel. Since our *fitness* function is minimized when the spectral output is maximum in a single channel of an specified width, it was proved that the multisoliton fission scenario is not expected to provide the best individual when using our GA. The same optimization method provides the optimum input pulse parameters required to control the SC dynamics in a way that the first two ejected Raman solitons are centered at two pre-defined wavelengths. The results are shown to be of interest for practical OCT applications in the NIR II region where dual frequency, pulsed sources enable in vivo imaging, and avoid spurious results.

Finally, it has been presented a well defined and efficient optimization procedure to obtain a shaped spectral output based on SC generation. This optimization is achieved with the use of pre-defined genetic algorithm functions. An ultra-flat spectrum was achieved numerically to prove the functionality of the method using commercial laser parameters and a standard single mode fiber based mainly on self-phase modulation effects, i.e., with the appropriate fiber,

laser source, and fitness function it is possible to obtain shaped spectral output with our method.

With this work, it is shown how SC spectra can be tailored with the described methods, resulting in a useful tool with great potential for optimization of the output of SC spectra for practical applications. This thesis has revealed many promising areas of further research in optimization of SC field. It has been shown that the optimization can be achieved using cheap computational systems and the adequate GA, until complex and expensive computational structures like GRID platforms. Then, the combination of the GA methodology with the use of GRID platform, and an appropriate theoretical analysis technique is therefore desirable. It is regarded as the further work of this project.

Appendix A

Published and In-Process Papers

Published Papers

F. R. Arteaga-Sierra, C. Milián, I. Torres-Gómez, M. Torres-Cisneros, A. Ferrando, and A. Dávila, *"Multi-peak-spectra generation with Cherenkov radiation in a non-uniform single mode fiber,"* Opt. Express **22**, 2451-2458 (2014).

F. R. Arteaga-Sierra, C. Milián, I. Torres-Gómez, M. Torres-Cisneros, G. Moltó, and A. Ferrando, *"Supercontinuum optimization for dual-soliton based light sources using genetic algorithms in a Grid platform,"* Opt. Express **22**, 23686-23693 (2014).

Submitted Paper

F. R. Arteaga-Sierra, C. Milián, I. Torres-Gómez, M. Torres-Cisneros, G. Moltó, and A. Ferrando, *"Optimization for maximum Raman frequency conversion as a tunable optical source using genetic algorithms implemented in a Grid platform,"* submitted to Laser Physics.

Paper in preparation

F. R. Arteaga-Sierra, I. Torres-Gómez, and M. Torres-Cisneros, *"Utra-flat supercontinuum spectrum by optimizing the zero dispersion wavelength profile in a tapered fiber using genetic algorithms,"* to be submitted to Optical Review.